Three-Dimensional Analysis of Geogrid-Reinforced Soil Using a Finite-Discrete Element Framework

V. D. H. Tran[1]; M. A. Meguid, M.ASCE[2]; and L. E. Chouinard[3]

Abstract: Three-dimensional analysis of soil-structure interaction problems considering the response at the particle scale level is a challenging numerical modeling problem. An efficient framework that takes advantage of both the finite- and discrete-element approaches to investigate soil-geogrid interactions is described in this paper. The method uses finite elements to model the structural components and discrete particles to model the surrounding soil to reflect the discontinuous nature of the granular material. The coupled framework is used in this study to investigate two geotechnical engineering problems, namely, strip footing over geogrid-reinforced sand and geogrid-reinforced fill over a strong formation containing void. The numerical model is first validated using experimental data and then used to provide new insights into the nature of the three-dimensional interaction between the soil and the geogrid layer. **DOI: 10.1061/(ASCE)GM.1943-5622.0000410.** © *2014 American Society of Civil Engineers.*

Author keywords: Geogrid reinforcement; Finite-discrete element; Strip foundation; Fill system over void.

Downloaded from ascelibrary.org by McGill University on 08/08/16. Copyright ASCE. For personal use only; all rights reserved.

Introduction

Continuum approaches [e.g., FEM and finite-difference method] are generally used for the analysis of soil-structure interaction problems. The FEM has proven to be a powerful tool in modeling both structural elements and the surrounding soil. Although the FEM can be used efficiently to model soil behavior at the macroscopic scale, capturing the discontinuous nature of the soil particles continues to be a challenging task. This discontinuous nature has an important role in the behavior of various soil-structure interaction systems such as soil-geogrid interlocking (McDowell et al. 2006), soil arching in embankments (Jenck et al. 2009; Han et al. 2012), and particle erosion in the vicinity of subsurface structures (Meguid and Dang 2009). The discrete-element method (DEM) proposed by Cundall and Strack (1979) is an alternative approach for modeling these systems. While the DEM can efficiently capture the discontinuous behavior of soils (Maynar and Rodríguez 2005; Lobo-Guerrero and Vallejo 2006; Tran et al. 2014; Lin et al. 2013), using discrete elements (DEs) to model structural components can lead to inaccurate response prediction. Research including McDowell et al. (2006), Han et al. (2012), Chen et al. (2012), and Ferellec and McDowell (2012) used sets of discrete particles bonded together to model structural components in a given system. However, because microvoids will generally exist in structural elements modeled using bonded particles, the continuous nature of these elements may not be fully captured.

To take advantage of both the FEM and DEM, the structure can be modeled using finite elements (FEs), whereas the soil can be modeled using DEs. The coupling of the two methods allows for both the soil and the structure to be simultaneously modeled. Elmekati and El Shamy (2010) used this approach to model pile installation in granular soil in which the pile was modeled using FEs while the surrounding soil was modeled using DEs. Dang and Meguid (2013) studied the earth pressure distribution on underground tunnels by modeling the structure of the tunnel lining using FEs and the surrounding soil using DEs. The analysis of geotextile-reinforced embankment using a coupled framework was reported by Villard et al. (2009). The soil-geogrid interaction during pullout loading was studied by Tran et al. (2013).The actual geogrid geometry was replicated using FEs, whereas the backfill soil was modeled using DEs. The soil-geogrid interaction was ensured using interface elements. In this study, a coupled FE-DE framework that is capable of modeling soil-structure interaction problems at the microscopic scale level is described and used to investigate two selected soil-geogrid interaction problems involving (1) the foundation over reinforced soil and (2) a geogrid-reinforced system spanning the subsurface void. Modeling of these problems allows for the merits of the soil-geogrid interlocking effect to be demonstrated. In addition, the stresses and displacements in the geogrid, contact orientation, contact forces between particles, particle movement, and change of soil porosity are also investigated. The literature review relevant to the investigated problems is provided in the corresponding sections.

Coupled FE-DE Framework

The coupled FE-DE framework presented in this study is a continuation of the original work of Dang and Meguid (2010b, 2013) and Tran et al. (2013, 2014). The framework is implemented into *YADE 0.97*—an open-source DE code (Han et al. 2012; Kozicki and Donze 2009; Šmilauer et al. 2010). The developed algorithm is briefly described in the subsequent sections.

[1]Graduate Student, Dept. of Civil Engineering and Applied Mechanics, McGill Univ., 817 Sherbrooke St. West, Montreal, QC, Canada H3A 0C3. E-mail: viet.tran@mail.mcgill.ca

[2]Associate Professor, Dept. of Civil Engineering and Applied Mechanics, McGill Univ., 817 Sherbrooke St. West, Montreal, QC, Canada H3A 0C3 (corresponding author). E-mail: mohamed.meguid@mcgill.ca

[3]Associate Professor, Dept. of Civil Engineering and Applied Mechanics, McGill Univ., 817 Sherbrooke St. West, Montreal, QC, Canada H3A 0C3. E-mail: luc.chouinard@mcgill.ca

Note. This manuscript was submitted on April 9, 2013; approved on April 15, 2014; published online on May 13, 2014. Discussion period open until October 13, 2014; separate discussions must be submitted for individual papers. This paper is part of the ***International Journal of Geomechanics***, © ASCE, ISSN 1532-3641/04014066(19)/$25.00.

FEs

In the coupled framework, FE analysis is performed using a dynamic relaxation approach. The general equation of the dynamic method is

$$\mathbf{K}\mathbf{x} + c\mathbf{M}\dot{\mathbf{x}} + \mathbf{M}\ddot{\mathbf{x}} = \mathbf{P} \tag{1}$$

where $\mathbf{M}$ = mass matrix; $\mathbf{K}$ = stiffness matrix; $\mathbf{P}$ = external force vector; $\mathbf{x}$ = displacement vector; and c = damping coefficient.

To satisfy the convergence condition, the time step, Δt_{FE}, must be smaller than a maximum time step $[\Delta t_{\mathrm{FE}}]$ determined by

$$[\Delta t_{\mathrm{FE}}] = \frac{2}{\sqrt{\lambda_m}} \tag{2}$$

where λ_m = maximum eigenvalue calculated using the element consistent tangent stiffness

$$\lambda_m \le \max_i \sum_{j=1}^{n} \frac{|K_{ij}|}{M_{ii}} \tag{3}$$

where M_{ii} = element of the diagonal mass matrix; and K_{ij} is an element of the global tangent stiffness matrix.

Discrete Elements

The interaction between DE particles is a dynamic process based on a time-stepping algorithm with an explicit finite-difference scheme. Because a dynamic approach is also used in FE analysis, it is possible to couple the two compatible approaches. In the DEM, the particle motion is determined using Newton's and Euler's equations. Energy from particle interactions is dissipated using damping coefficients. The convergence condition is satisfied when all internal and external forces are balanced. The interaction between two DE particles is determined using contact laws. The contact law used in this study is briefly described subsequently [Fig. 1(a)].

The interaction between two particles, A and B, is represented by normal force $\mathbf{F}_N$, tangential force $\mathbf{F}_T$, and rolling resistance moment $\mathbf{M}_r$. The normal and tangential contact forces are determined using the normal penetration between the two particles, Δ_N, and incremental tangential displacement, $\delta\Delta_T$, such that

$$\mathbf{F}_N = K_N \cdot \boldsymbol{\Delta}_N \tag{4a}$$

$$\delta\mathbf{F}_T = -K_T \cdot \delta\boldsymbol{\Delta}_T \tag{4b}$$

where K_N and K_T = normal and tangential stiffnesses at the contact, respectively, which are defined by

$$K_N = \frac{2E_A r_A E_B r_B}{E_A r_A + E_B r_B} \tag{5}$$

and

$$K_T = \alpha K_N \tag{6}$$

where E = particle material modulus; r = particle radius; and α = constant ratio.

The rolling resistance moment, $\mathbf{M}_r$, is introduced to represent the rolling restraint between the two interacting particles. Here, $\mathbf{M}_r$ is calculated using a rolling angular vector, θ_r, which describes the relative orientation change between the two particles by summing the angular vectors of the incremental particle rolling.

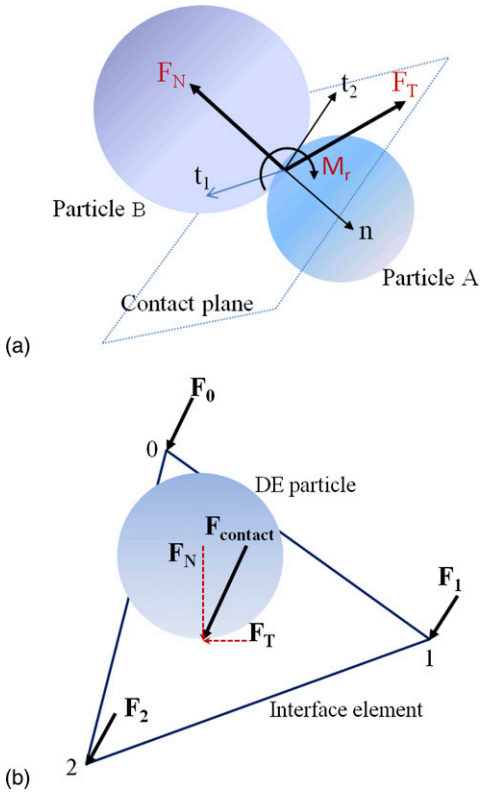

Fig. 1. (a) Interaction between two DE particles; (b) forces transmitting to FE nodes through DE particle-interface element interaction

Both tangential force $\mathbf{F}_T$ and moment $\mathbf{M}_r$ are limited by a threshold value such that

$$\mathbf{F}_T = \frac{\mathbf{F}_T}{\|\mathbf{F}_T\|}\|\mathbf{F}_N\|\tan(\phi_{\mathrm{micro}}) \quad \text{if} \quad \|\mathbf{F}_T\| \ge \|\mathbf{F}_N\|\tan(\phi_{\mathrm{micro}}) \tag{7}$$

and

$$\mathbf{M}_r = \begin{cases} K_r\boldsymbol{\theta}_r & \text{if} \quad K_r\|\boldsymbol{\theta}_r\| < \|\mathbf{M}_r\|_{\mathrm{lim}} \\ \|\mathbf{M}_r\|_{\mathrm{lim}}\dfrac{\boldsymbol{\theta}_r}{\|\boldsymbol{\theta}_r\|} & \text{if} \quad K_r\|\boldsymbol{\theta}_r\| \ge \|\mathbf{M}_r\|_{\mathrm{lim}} \end{cases} \tag{8}$$

where

$$\|\mathbf{M}_r\|_{\mathrm{lim}} = \eta_r\|\mathbf{F}_N\|\frac{r_A + r_B}{2} \tag{9}$$

where K_r = rolling stiffness of the interaction computed by

$$K_r = \beta_r\left(\frac{r_A + r_B}{2}\right)^2 K_T \tag{10}$$

where β_r = rolling resistance coefficient; and η_r = dimensionless coefficient.

Interface Elements

Interface elements are implemented to model the interaction between the FE and DE domains. Because triangular facets are capable of reproducing complex surfaces they are adopted in this study as interface elements. A triangular facet is directly defined by three common nodes

Downloaded from ascelibrary.org by McGill University on 08/08/16. Copyright ASCE. For personal use only; all rights reserved.

of the element between the FE and the interface if the element has a triangular or a tetrahedron shape. In the case of quadrilateral or hexahedral elements, the contact interface is divided into four triangular facets by creating a temporary center node determined by

$$x^{(O)} = \frac{1}{4}\sum_{i=1}^{4} x^{(i)} \tag{11}$$

where $x^{(i)}$ = coordinate of node i of the quadrilateral.

The particle-interface interaction is schematically illustrated in Fig. 1(b). The contact algorithm used for this interaction is similar to that described previously between discrete particles, where a set of potential contacts between particles and interface elements is first obtained through spatial sorting. The particle-interface contact is then determined based on the separation distance as well as the projection position of the particle center on the interface element. Normal penetration Δ_N and incremental tangential displacement $\delta\Delta_T$ are determined, which allows for the normal and tangential contact forces to be calculated [Eqs. (4*a*) and (4*b*)]. The interaction forces transmitted to the FE nodes can then be determined as follows:

$$\mathbf{F}_i = \mathbf{F}_{\text{contact}} \cdot N_i \tag{12}$$

where $\mathbf{F}_{\text{contact}} = \mathbf{F}_N + \mathbf{F}_T$ is the total contact force; and N_i = shape functions obtained using the natural coordinates of the contact point.

It is not efficient to use a common time step for both FE and DE models because the time step (Δt_{FE}) required for FEs is much larger than that for DEs (Δt_{DE}). Thus, different time steps for each domain are implemented in the coupling framework to improve the computational efficiency. The time step in the FE domain is selected as $\Delta t_{\text{FE}} = n\Delta t_{\text{DE}}$, where n is an integer such that $n \leq [\Delta t_{\text{FE}}]/\Delta t_{\text{DE}}$. This is implemented by executing the FE solver for every n DE computation. A similar multiple-time-step algorithm is also described in Xiao and Belytschko (2004) and Elmekati and El Shamy (2010).

The calculation steps in a typical cycle are summarized as follows: (1) potential interactions among DE particles and between DEs and interface elements are determined; (2) contact parameters of each interaction are determined using the corresponding contact laws; (3) interaction forces between DE particles and between DEs and interface elements are calculated; and (4) particle velocities and positions are determined. For every n time steps, the FE solver is executed and the forces acting on the FE nodes are updated to determine the node displacements.

Geogrid-Reinforced Foundation

Over the past three decades, the use of geosynthetics to increase the bearing capacity of shallow foundations has received extensive research attention. The bearing capacity of reinforced soil has been studied experimentally by many researches, including Guido et al. (1986), Huang and Tatsuoka (1990), Khing et al. (1993), Shin et al. (1993), Das et al. (1994), Yetimoglu et al. (1994), Adams and Collin (1997), Dash et al. (2001), DeMerchant et al. (2002), Patra et al. (2006), Basudhar et al. (2007), Chen et al. (2007), Abu-Farsakh et al. (2008), Ghazavi and Lavasan (2008), Chen et al. (2009), Ghosh and Dey (2009), Madhavi Latha and Somwanshi (2009a, b), Sadoglu et al. (2009), Choudhary et al. (2010), Mohamed (2010), and Moghaddas Tafreshi and Dawson (2010). Although geogrid reinforcement is not commonly used in practice to reinforce shallow foundations, these experimental studies have demonstrated the efficiency of geosynthetic material in increasing the bearing capacity of shallow foundations. The effects of different variables such as geosynthetic length, vertical spacing between multiple reinforcing layers, depth to the top layer, number of layers, and types of geosynthetics that contribute to the bearing capacity were examined. Analytical solutions were also developed by Binquet and Lee (1975a, b), Huang and Menq (1997), Wayne et al. (1998), Kumar and Saran (2003), Michalowski (2004), Abu-Farsakh et al. (2008), Sharma et al. (2009), and Chakraborty and Kumar (2014). Numerical analysis is an alternative way to study the stresses and strains within a given soil-geosynthetic system. The FE modeling of reinforced foundations has been reported by Yetimoglu et al. (1994), Kurian et al. (1997), Siddiquee and Huang (2001), Yamamoto and Otani (2002), Basudhar et al. (2007), Chung and Cascante (2007), Ghazavi and Lavasan (2008), Madhavi Latha and Somwanshi (2009a, b), and Li et al. (2012). In these studies, modeling the reinforcement layer was often simplified either by using truss elements [in two-dimensional (2D) analysis] or a continuous sheet [in three-dimensional (3D) analysis]. This simplification does not necessarily represent the true geometry of geosynthetic reinforcing layers, particularly for geogrids. In addition, the interaction between simplified geogrid models and the surrounding soil was often captured using interface elements in which the contact properties were considered while the interlocking effect was not generally represented. It is known that soil-geogrid interlocking plays an important role in the load-carrying capacity of foundations over geogrid-reinforced soils (Guido et al. 1986). The interlocking of the soil particles through the grid apertures mobilizes the tensile strength in the reinforcing layer and generates an anchoring effect that leads to better geotechnical performance. Modeling such interactions considering continuous geosynthetics sheets has been reported by Villard et al. (2009) using the FE-DE method. The coupled approach presented in this study allows for the interlocking effect to be explicitly simulated by considering the soils as DEs while the 3D geometry of the geogrid is represented using FEs. The interaction between the two domains is ensured by using interface elements. Additional modeling details are provided subsequently.

Model Generation

In this study, the experimental results reported by Das et al. (1994) and Khing et al. (1993) for a strip footing supported by geogrid-reinforced sand is used to validate the proposed coupled FE-DE model. The soil container was reported to be 1.1 m in length, 0.3 m in width, and 0.9 m in height. The interior wall surfaces were polished to reduce soil-wall friction. The strip footing had a width of 76 mm (noted as B) and a length of 300 mm. A rough condition at the base of the footing was generated by cementing a thin layer of sand at the contact surface. The soil used in the experiment was medium-grained silica sand with $D_{50} = 0.51$ mm, average dry unit weight of 17.14 kN/m^3, and a peak friction angle of 41° (at $D_r = 70\%$), obtained from laboratory direct shear tests. Biaxial geogrids (Tensar SS-0 with polypropylene/high-density polyethylene copolymer material and tensile modulus of 182 kN/m at 2% strain), 760 mm in length and 300 mm in width, were used in the experiments. The top geogrid layer was installed at a depth of 25 mm (0.33B) below the foundation base. The number of geogrid layers installed in the soil was varied and the distance between two adjacent layers was 25 mm (0.33B). The sand was placed in layers of 25 mm, each using a raining technique, and the geogrid was placed at predetermined locations. The model foundation was then placed on the soil surface and vertical loading was applied using a hydraulic jack. Given the previously described test procedure, the reported experimental results may overestimate the increase in bearing capacity of the foundation because of the fact that reduced scale footing was used in combination with prototype-scale geogrid reinforcement. However,

Downloaded from ascelibrary.org by McGill University on 08/08/16. Copyright ASCE. For personal use only; all rights reserved.

for the purpose of this study, the qualitative experimental data are deemed sufficient for validation of the numerical framework.

The numerical model was developed such that it follows the geometry and test procedure used in the experiment. Because of the high computational time required for the coupled FE-DE analysis, up to two geogrid layers were considered in this study. The geogrid was modeled using FEs while the soil was modeled using DEs, as discussed in the previous sections. Interface elements were used to capture the interaction between the two domains. All components were generated inside *YADE 0.97* using two corresponding FE and DE packages.

The biaxial SS-0 geogrid, which was comprised of 11 longitudinal elements and 21 transverse elements, was modeled using 8-node brick elements with eight integration points (Fig. 2). A linear elastic material model was used for the geogrid sheet. This assumption is considered appropriate because the observed geogrid deformation was relatively small. A Poisson's ratio of 0.3 was used for the geogrid material, as suggested by Liu et al. (2007) and Kwon et al. (2008). The Young's modulus of the geogrid was determined by matching the experimental load-displacement relationship based on the reported index test results at a strain rate of 2% (as shown in Table 1). The local increase in joint thickness was not considered in the geogrid model in order to simplify the numerical analysis. The full geometry of the geogrid, which was comprised of over 1,900 FEs and 29,000 interface elements, is shown in Fig. 2.

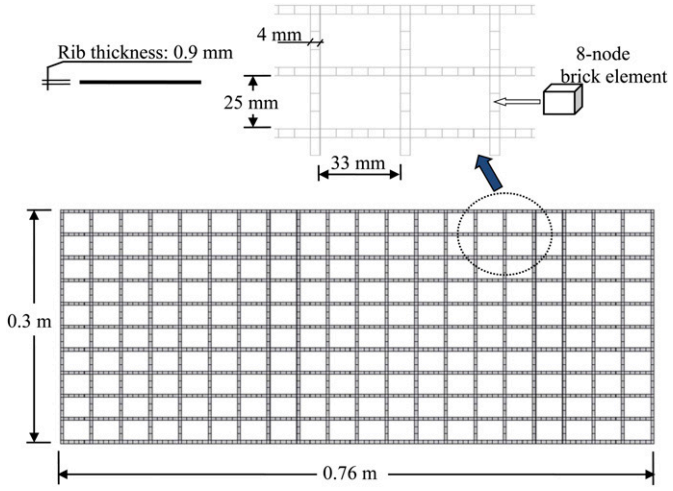

Fig. 2. Plan view of the geogrid sheet

Table 1. Input Parameters for the Simulation

Type of element	Parameter	Value
Discrete particle	Density (kg/m^3)	2,650
	Material modulus E (MPa)	38
	Ratio K_T/K_N	0.25
	Coefficient of friction ($\tan\phi_{micro}$)	0.68
	β_r	0.01
	η_r	1.0
	Damping coefficient	0.2
FE	Young's modulus E (MPa)	1.4×10^3
	Poisson's ratio ν	0.3
Interface element	Material modulus E (MPa)	38
	Ratio K_T/K_N	0.25
	Coefficient of friction ($\tan\phi$)	0.42

The sand used in the experiment was modeled using spherical particles. Because it is numerically prohibitive to simulate millions of particles with true sizes, particle upscaling was necessary to reduce the number of DEs used in the model. Consideration of particle size is usually made to maintain the balance between the computational cost and the scaling effects. In this study, the diameters of the used particles followed a normal distribution with a mean value of 10.2 mm (20 times the real D_{50}) and a SD of 2.0 mm.

To generate the DE samples, appropriate packing techniques were used to provide the best replication of the actual soil placement process. Several packing algorithms have been reported to generate DE specimens (Cundall and Strack 1979; Jiang et al. 2003; Labra and Oñate 2009; Dang and Meguid 2010a; Tran et al. 2014). In this study, the soil samples were generated by using the gravitational approach proposed by Tran et al. (2014) to represent the actual soil placement in layers under gravity, as will be described subsequently.

Thin layers of particles (each 0.05 m thick) were generated using the DE samples described previously. To build the first layer, a set of noncontacting particles was generated until the target volume was reached. This target volume was calculated based on a sand porosity of 0.36. The initial height of the box was chosen to be larger than the target height of the layer to ensure that all particles were generated without overlapping. Gravity was then applied to all particles, allowing them to move downward and to contact each other. The interparticle friction angle was initially set to zero. The generated sample was found to be looser than the actual sand, even when the friction angle was zero. To increase the density of the packing, lateral shaking was applied to the box to help small particles move into the voids located between larger particles. The generation of the first layer was considered to be completed when the equilibrium condition was reached. For the second layer, the height of the box was increased and a second cloud of noncontacting particles was generated in the area above the first layer. Gravity and shaking were then applied and the system was allowed to come into equilibrium. To introduce the geogrid layer at a given location, particles above the geogrid level were removed and both the geogrid and interface elements were generated. At this stage, the geogrid was assumed to be nondeformable in order to maintain its initial geometry during the sample generation process. A next cloud of particles was generated and the procedure was repeated until the final DE sample was reached. The generated assembly was then checked using the fabric tensor and contact orientation, as will be shown subsequently. The 3D geometry of the final DE sample with over 245,000 particles is shown in Fig. 3(a). A partial view of the particle-geogrid interaction is shown in Fig. 3(b). It can be seen that the interlocking of the soil through the apertures of the grid is properly simulated. Furthermore, particles from one side of the geogrid can interact directly with particles from the other side, which closely represents the real behavior of the soil-geogrid interaction.

The microscopic parameters used in the analysis were the following: a particle density of 2,650 kg/m^3; K_T/K_N ratio of 0.25; β_r of 0.01; and particle material modulus of 38 MPa, as suggested by Tran et al. (2014). The friction angles of the DE particles were determined by matching the numerical and experimental direct shear test results. The numerically simulated shear box (60×60 mm) was filled with the DE sample, which consisted of over 100,000 particles with a mean diameter of 1.0 mm (twice the actual D_{50}). The packing process described previously was used to generate the DE specimen in order to ensure consistency with the characteristics of the actual soil sample (Tran et al. 2014). The microscopic friction angle was varied incrementally to match the peak friction angle measured in the experiment. It was found that a friction coefficient ($\tan\phi_{micro}$) value of 0.68 provided the best agreement. Despite the differences in the particle sizes used in the numerical simulation and the actual direct shear test, the parameters obtained were found to produce a close

Downloaded from ascelibrary.org by McGill University on 08/08/16. Copyright ASCE. For personal use only; all rights reserved.

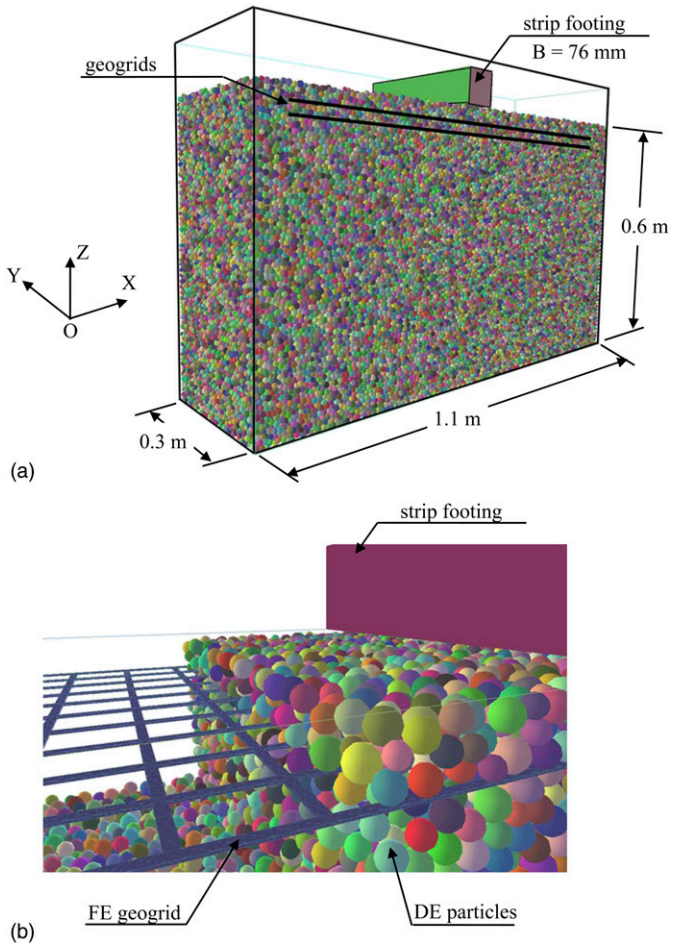

Fig. 3. (a) Initial geometry of the geogrid-reinforced footing; (b) partial view of the DE particle-geogrid interaction

representation of the real sand used in the experiments. The randomness of the generation process was found to have a minor effect on the macroscopic response because the number of particles in the DE specimen was large enough to capture the behavior of the sample (Tran et al. 2014).

Numerical Simulation

After the final specimen was generated, the strip footing (76 × 300 mm) was numerically simulated and initially placed at the soil surface [see Fig. 3(a)]. The input parameters given in Table 1 were then assigned to the discrete particles and FEs. No friction was used for the interior sides of the box walls, whereas a high friction angle with a tangent of 1.0 was applied for the interaction between the footing base and the DE particles in order to replicate the rough footing condition used in the experiments. A parametric study was conducted to examine the effect of the interaction between the DE particles and interface elements on the response of the modeled strip footing. The results indicated that the stiffnesses of the interface elements did not have a significant effect on the calculated response. Therefore, the stiffnesses of the interface elements were assigned values similar to those used for the DE particles. This is consistent with the findings of Villard et al. (2009) for similar geosynthetic-soil interaction problems. On the other hand, the coefficient of friction between the discrete particles and interface elements was found to affect the overall response of the soil-geogrid system, and therefore it needs to be determined using the available experimental data. This is attributed to the fact that spherical particles usually mobilize less frictional contact with structural surfaces than real sand particles. A parametric study was conducted to examine the effect of the particle-interface friction coefficient on the overall behavior of the footing system, and a friction coefficient of 0.42 was found to provide satisfactory results compared with the measured values.

Before the loads were applied to the foundation, the fabric tensor and contact orientations were investigated. The fabric tensor (Dang and Meguid 2010a) is determined by

$$\mathbf{\Phi}_{ij} = \frac{1}{N_c} \sum_{N_c} n_i n_j \tag{13}$$

where N_c = number of contacts; and n_i = unit branch vector component in the i-direction. The calculated fabric tensor components are nearly identical ($\mathbf{\Phi}_{xx} = \mathbf{\Phi}_{yy} \approx 0.33$ and $\mathbf{\Phi}_{zz} \approx 0.34$, where z is the gravitational direction). The distribution of contact orientations is shown in Fig. 4. It can be seen that the contacts are homogeneously distributed in all directions and contacts at angles of 0 and 90° appear to have privileged orientations. A similar observation was reported by Belheine et al. (2009).

After the aforementioned steps were completed, the geogrids were allowed to freely deform and the footing pressure was applied in small increments by using a stress control mechanism. For each loading stage, when the current pressure, σ, differed from the target value, σ_v, the footing moved vertically to a distance of $dz = (\sigma - \sigma_v)/K$, where stiffness K was determined by adding the normal stiffnesses of all active particle-footing interactions. This loading process allows for a constant pressure to be maintained. For each load increment, the applied pressure was kept constant until the convergence conditions were satisfied in both the DE and FE domains.

Results and Discussion

Validation of the Numerical Model

In this section, the effect of introducing one or two geogrid reinforcement sheets into the soil is examined and compared with the unreinforced case. To validate the numerical model, the coupled FE-DE analysis results are compared with the experimental data. Fig. 5 shows the relationship between the applied footing pressure and the vertical settlement for three cases: no reinforcement ($N = 0$), one geogrid layer ($N = 1$), and two geogrid layers ($N = 2$). In Fig. 5 it can be seen that the calculated responses in all cases agree well with the experimental data. For a given settlement value, the load-carrying capacity increased when geogrid reinforcement was introduced. The ultimate bearing capacity also increased with the addition of a second geogrid layer ($N = 2$). The ultimate bearing capacity calculated by Das et al. (1994) was also consistent with the numerically calculated results using the proposed numerical framework.

Response of the Geogrids

The deformed shapes of the geogrid layers for a given footing pressure are shown in Fig. 6. A reference pressure value ($q = 125$ kPa) that was smaller than the ultimate capacity for $N = 1$ was chosen because it allowed for the displacements in the two cases ($N = 1$ and 2) to be examined. The vertical displacements of the cases of $N = 1$ and 2 are shown in Figs. 6(a and b), respectively, where it can be seen that the vertical displacement of $N = 1$ is generally larger than that for $N = 2$. In addition, the vertical displacement of the upper geogrid sheet is larger

Downloaded from ascelibrary.org by McGill University on 08/08/16. Copyright ASCE. For personal use only; all rights reserved.

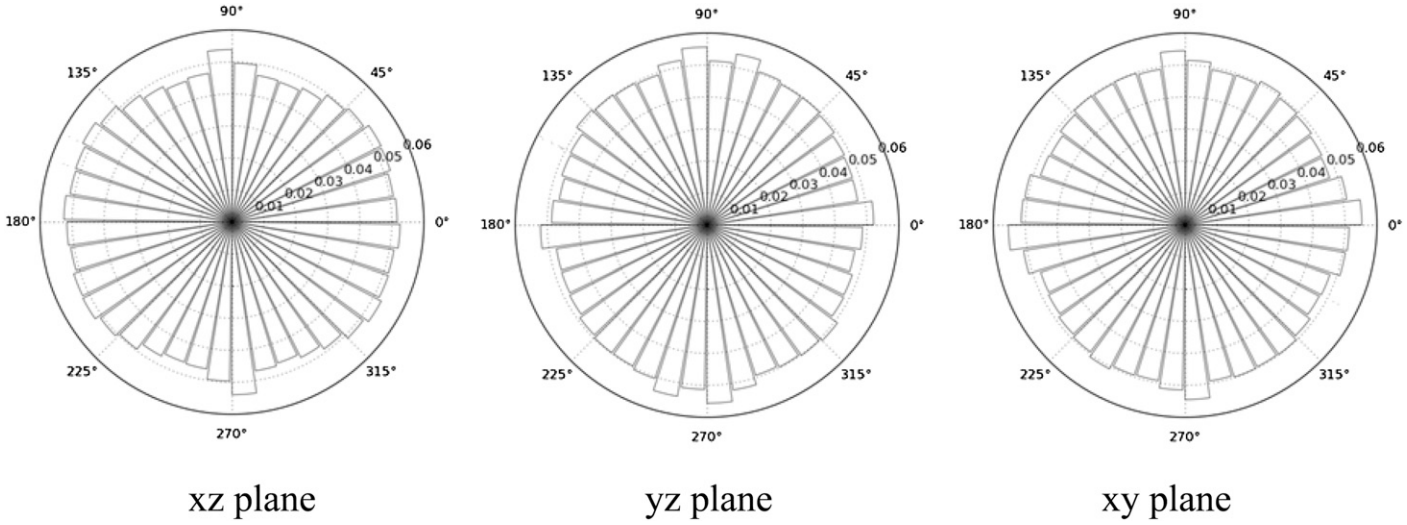

Fig. 4. Distributions of the contact orientation at the initial condition

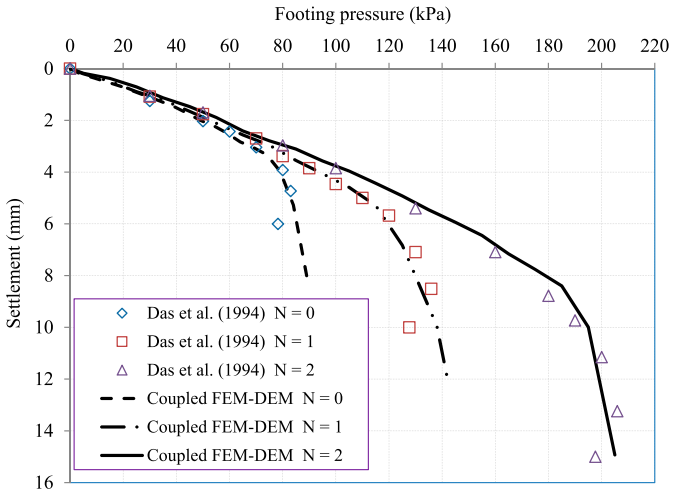

Fig. 5. Load-settlement curves of the geogrid-reinforced foundation system

than that of the lower one for the case of two reinforcement layers. Consistent with the displacement pattern, the tensile stresses in the geogrid for $N = 1$ were found to be larger than that for $N = 2$, as shown in Fig. 7. For the $N = 2$ case, the upper geogrid layer experienced higher tensile stresses compared with that in the lower layer. In both cases, the deformations of the geogrids occurred mainly in the area immediately below the footing, whereas very small deformations developed away from that area. Similarly, the stresses (S_{xx}) developing in the geogrid reached the highest values right under the footing location and decreased with distance away from the loaded area. The vertical displacement and tensile stress distributions of the $N = 1$ case are shown in Fig. 8, where it can be seen that the vertical displacements and tensile stresses of the geogrid occur within a distance of $1.5B$ from the foundation center and become negligible outside this region. The maximum calculated vertical displacements and tensile stresses in the geogrid for various footing pressures are shown in Fig. 9, where it is observed that for a given footing pressure the vertical displacements and tensile stresses in the geogrid are larger for $N = 1$ than for $N = 2$. Figs. 9(a and b) also illustrate that for the $N = 2$ case, the deformation and tensile stresses developing in the upper geogrid layer are generally larger than that experienced by the lower layer.

Response of the Reinforced Soil

The displacement field within the unreinforced soil at the ultimate bearing capacity is shown in Fig. 10, where it can be seen that a general shear failure mode occurs and extends to a depth of $D = 1.2B$. Negligible soil displacements are observed outside a region that extends laterally $3B$ from the foundation center line. The displacement fields of the reinforced foundation for $N = 1$ prior to and at failure are shown in Fig. 11(a and b), respectively, where it can be seen that prior to failure [Fig. 11(a)], the horizontal displacement below the geogrid layer is small compared with the vertical displacement component at the same location. At peak loading [Fig. 11(b)], a punching shear failure pattern occurs above the geogrid followed by a general shear failure below the geogrid. With the shear band development under the footing, the displacement field at peak loading was limited to the failure zone dominated by the horizontal and upward movements. This failure mode was also reported by Meyerhof and Hanna (1978) and Wayne et al. (1998) for a strong soil layer overlaying a weaker soil. Similar observations were made by Schlosser et al. (1983), Huang and Tatsuoka (1990), and Huang and Menq (1997) for a deep footing mechanism, where the frictional and interlocking forces as a result of the interaction between the soil and geogrids resulted in an increase in the soil compressive strength, and thus an increase in the bearing capacity of the reinforced soil. Similar soil deformation patterns were recorded by Michalowski and Shi (2003), who used a digital motion detection technique.

The contact force network within the soil domain with and without geogrid reinforcement is shown in Fig. 12. The contact force distributions represent the transmission of the applied load to the supporting soil. Each contact force is illustrated by a line connecting the centers of two contacting elements while the width of the line is proportional to the magnitude of the normal contact force. It can be seen in Figs. 12(a–c) that large contact forces develop immediately beneath the strip footing for $N = 0$, 1, and 2, respectively. It can also be seen in Fig. 12(a) that the contact force network of unreinforced

Downloaded from ascelibrary.org by McGill University on 08/08/16. Copyright ASCE. For personal use only; all rights reserved.

Downloaded from ascelibrary.org by McGill University on 08/08/16. Copyright ASCE. For personal use only; all rights reserved.

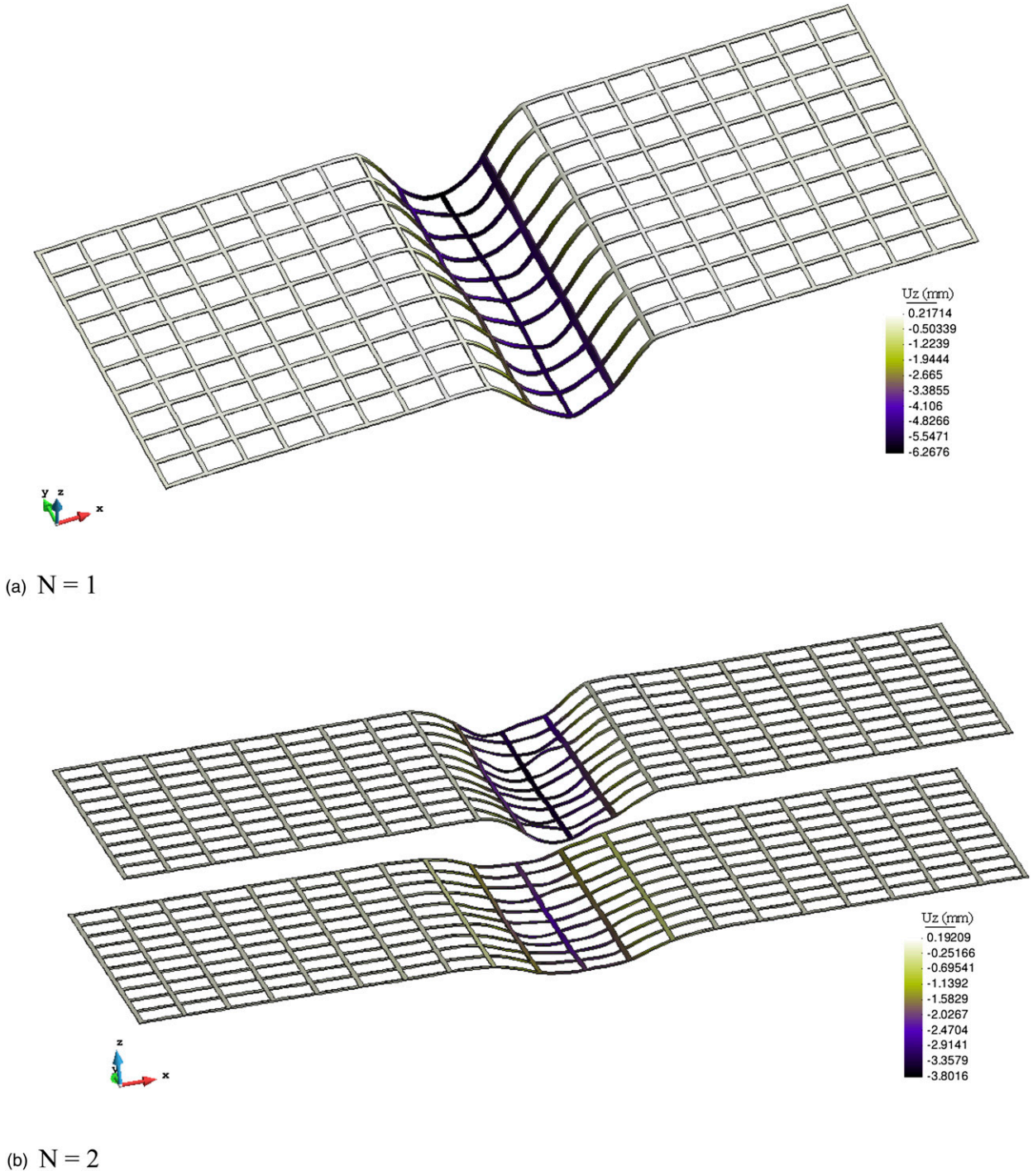

Fig. 6. Vertical displacement of the geogrid at a given foundation pressure $q = 125$ kPa: (a) one geogrid layer; (b) two geogrid layers

soil develops diagonally from the footing base. As seen in Figs. 12(b and c), with the presence of reinforced geogrid layers the contact forces become more vertical, particularly above the location of the geogrid layers. Below the geogrid, diagonal contact forces are found, which are similar to those observed beneath the unreinforced case. The contact force distributions shown in Fig. 12 support the failure mode discussed previously.

To calculate the macroscopic stress components within the soil domain, averaging windows with dimensions $S_x \times Sy \times S_z = 0.05 \times 0.3 \times 0.025$ m were used. The average stresses within a given box are given by

$$\sigma_{ij} = \frac{1}{V} \sum_{c=1}^{N_c} x^{c,i} f^{c,j} \tag{14}$$

where N_c = number of contacts within the box of volume V; $f^{c,j}$ = contact force vector at contact c; $x^{c,i}$ = branch vector connecting two contact particles, A and B; and indices i and j = Cartesian coordinates.

The distribution of vertical stresses with depth beneath the center of the footing is shown in Fig. 13. Consistent with the large vertical contact forces developing above the geogrids (Fig. 12), an increase

Downloaded from ascelibrary.org by McGill University on 08/08/16. Copyright ASCE. For personal use only; all rights reserved.

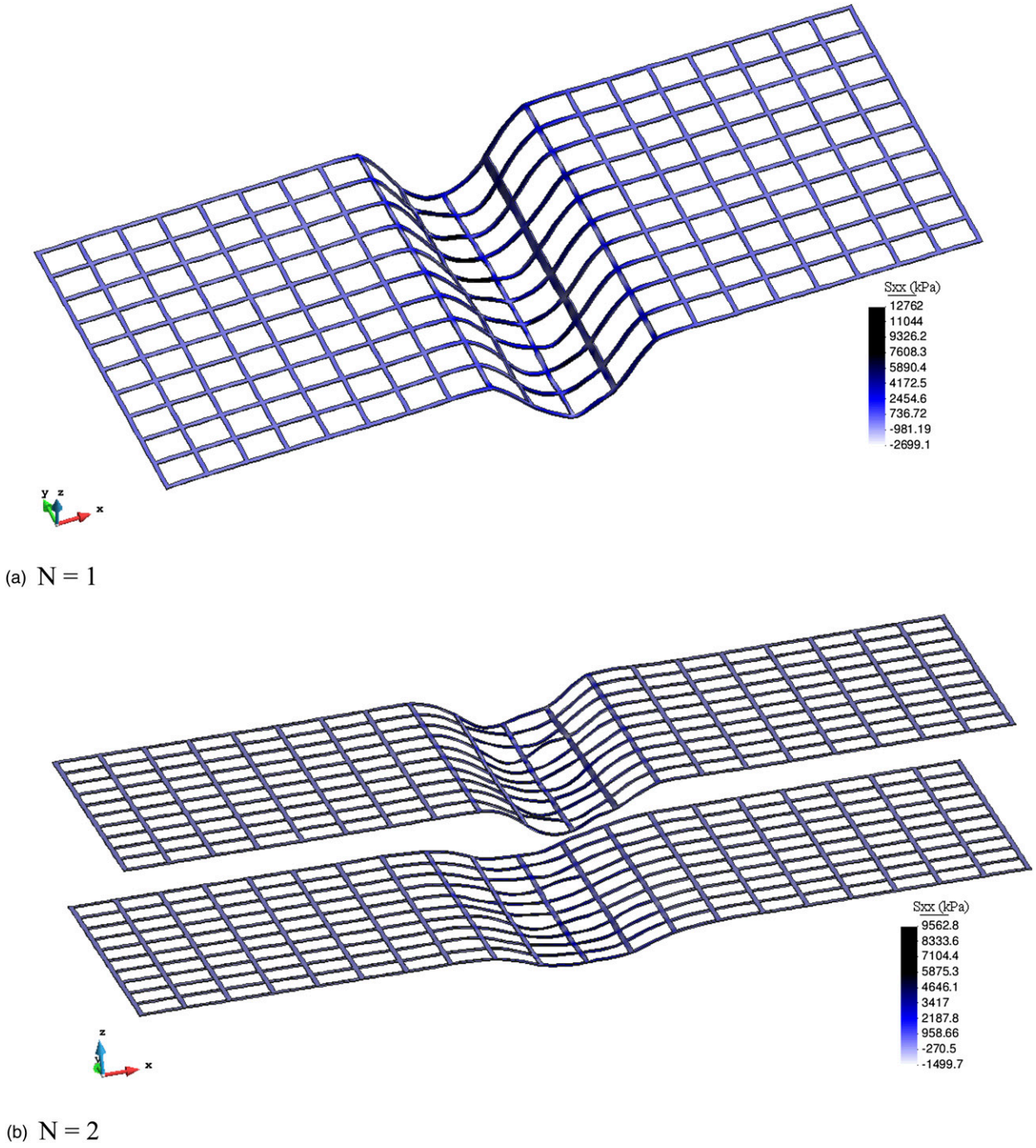

Fig. 7. Geogrid stress S_{xx} at a reference foundation pressure $q = 125$ kPa: (a) one geogrid layer; (b) two geogrid layers

in vertical stresses within this zone is also observed. The increase in the number of geogrid layers resulted in an increase in vertical stresses. However, no significant changes in vertical stresses were found beyond a depth of $1.2B$ below the geogrids. A similar observation was reported by Jeon (2011). The previously described vertical stress distribution was consistent with the calculated displacement fields (Fig. 11) and contact force networks (Fig. 12).

Geogrid-Reinforced Fill over Void

Fill structures such as embankments and highways are often constructed on natural ground that is susceptible to erosion. Therefore, cavities may develop under an existing embankment during its service life. This is particularly true in coral and karstic formations or in rock with soft inclusions (Agaiby and Jones 1995). These voids can cause severe damage to overlying and nearby structures. This condition was first considered by Terzaghi (1936) and is known as the trap door problem. A rigid trap door located at the base of a soil-filled container was lowered, causing soil arching and movement into the generated void. Numerical modeling of the trap door problem using the FEM was reported by Koutsabeloulis and Griffiths (1989). To prevent sudden failure, reinforcement layers are usually installed at the base of embankments constructed over subsurface soils that are susceptible to erosion. Reinforcement layers that bridge over voids are known

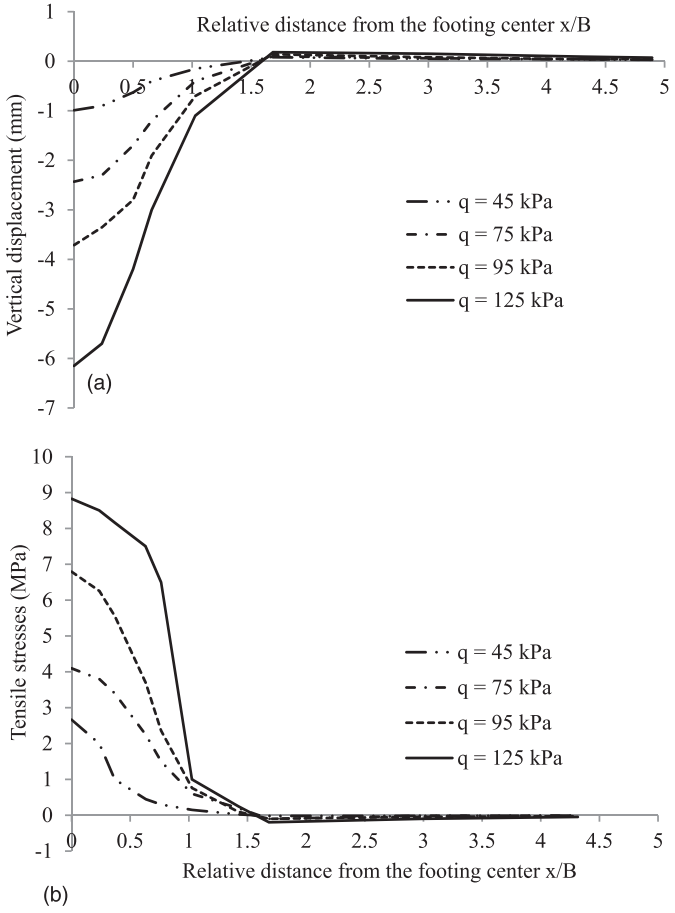

Fig. 8. (a) Vertical displacements of the geogrid ($N = 1$); (b) tensile stresses of the geogrid ($N = 1$)

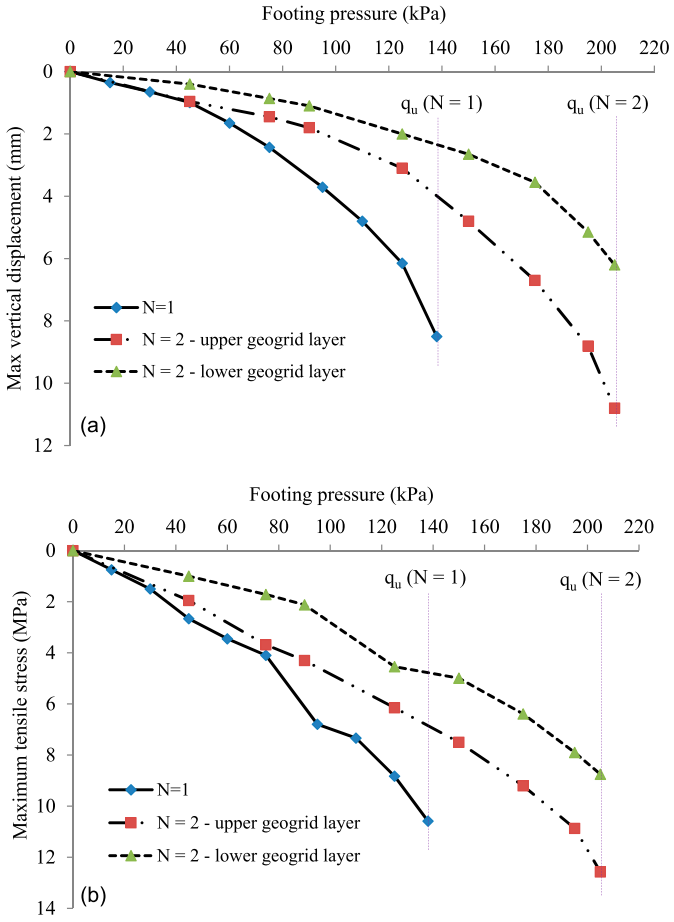

Fig. 9. (a) Maximum vertical displacements of the geogrids; (b) maximum tensile stresses in the geogrids

to reduce settlements and protect against failure of the overlying structure. Kinney and Connor (1987) conducted field tests to investigate the performance of road embankments over voids. The results suggested that geosynthetics can be beneficial when a fill material is placed over a location with subsurface voids. The ability of geogrid-reinforced pavements to provide an early warning system beneath a road embankment was reported by Bridle et al. (1994). The efficiency of installed geosynthetic reinforcements over sinkholes was investigated by Villard et al. (2000) and Moghaddas Tafreshi et al. (2011). Analytical solutions for reinforced systems over voids were also reported by Giroud et al. (1990), Poorooshasb (1991), Agaiby and Jones (1995), Wang et al. (1996), Villard et al. (2000), and Briançon and Villard (2008). The FE-DE analyses of reinforced systems were reported by Gabr et al. (1992), Gabr and Hunter (1994), Lawson et al. (1994), Agaiby and Jones (1995), Wang et al. (2009), Gaetano (2010), Jones et al. (2010), and Halvordson et al. (2010). In most cases, only 2D models were used, and therefore the 3D geometry of the geosynthetic material was not represented. The DEM has been used to model geogrid-reinforced embankments over piles (Han et al. 2012); however, a simplified 2D geometry of the geogrid was adopted. It has been also shown that (Bridle et al. 1994) for this class of problems, the particle interlocking mechanism leads to the formation of a stiffened layer above the void, which prevents collapse of the overlying system. Therefore, a simplified 2D model of the geogrid geometry may misrepresent the behavior of such reinforced earth structures. In this study, a fill placed on a geogrid layer spanning an induced subsurface void was numerically simulated using the coupled FE-DE framework. The proposed method allows for both the 3D geometry of the geogrid and the interlocking mechanism associated with the soil-geogrid interaction to be represented.

Model Generation

A condition simulating granular fill material reinforced with geogrid overlying an induced void is analyzed in this section using the coupled FE-DE framework. The numerical analysis aims at investigating the interaction between the geogrid and the supported soil as a result of the introduction of small subsurface voids. The thickness of the fill layer was 0.6 m, placed over a strong rigid foundation with an induced cavity (0.2-m width, 0.3-m height), as shown in Fig. 14. Previous studies (Giroud et al. 1990; Poorooshasb 1991; Agaiby and Jones 1995; Wang et al. 1996; Villard et al. 2000; Briançon and Villard 2008) assumed that geosynthetic reinforcement layers are installed directly over the rigid surface. Although this assumption simplifies the numerical analysis, it does not necessarily cover all possible cases. The geogrid was simulated using FEs while the fill (and the underlying soil) was simulated using DEs. The rigid subsurface formation hosting the cavity was modeled as a nondeformable FE domain. The geogrid placement directly over the rigid formation was found to cause numerical instability unless additional restraints were applied to the geogrid. These restraints prevented the geogrid from deforming laterally, and therefore affecting the soil-geogrid frictional resistance and interlocking mechanism. To ensure proper interaction between the geogrid and

Downloaded from ascelibrary.org by McGill University on 08/08/16. Copyright ASCE. For personal use only; all rights reserved.

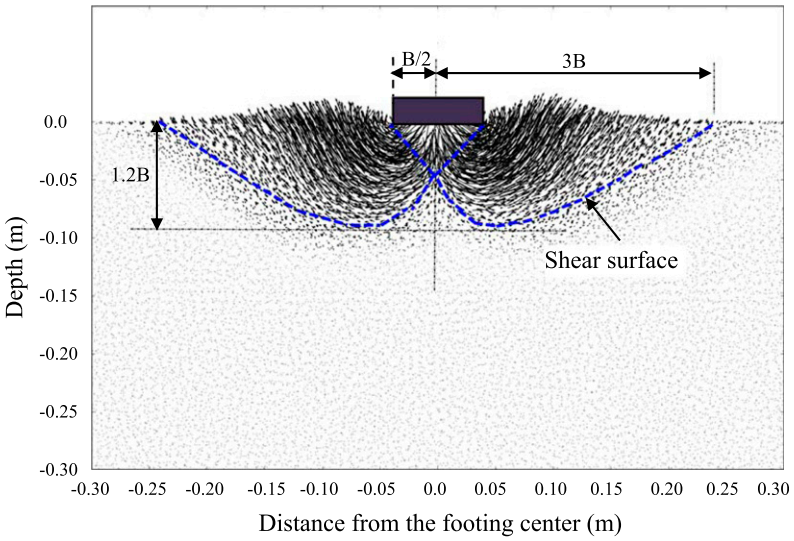

Fig. 10. Displacement field in the unreinforced soil

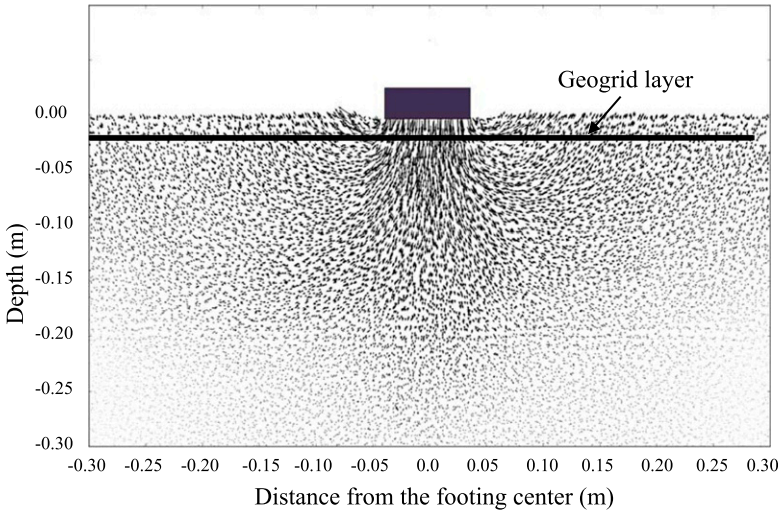

(a) Before failure - N = 1

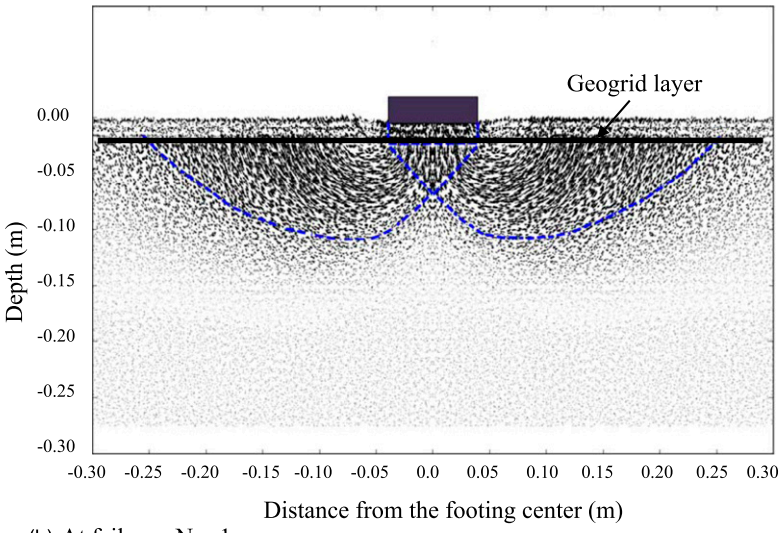

(b) At failure - N = 1

Fig. 11. Displacement field in the reinforced soil ($N = 1$)

Downloaded from ascelibrary.org by McGill University on 08/08/16. Copyright ASCE. For personal use only; all rights reserved.

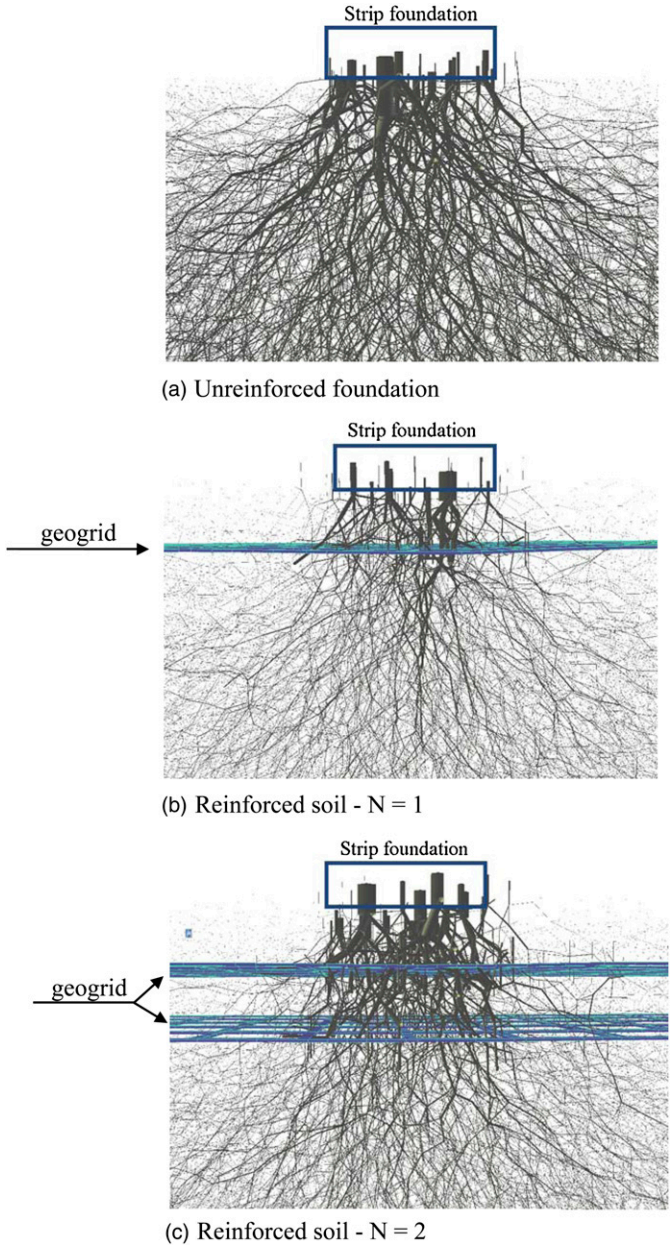

Fig. 12. Contact force networks within the foundation soil

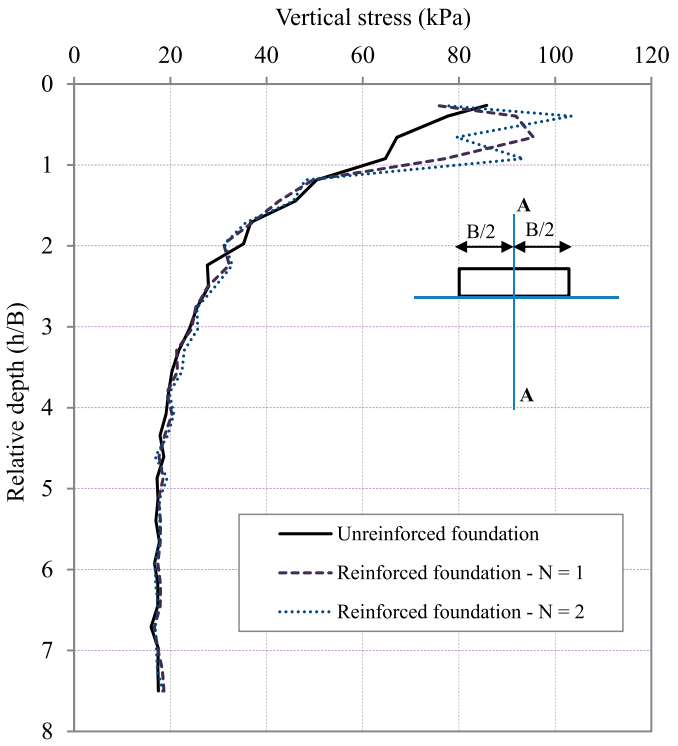

Fig. 13. Vertical stress distributions beneath the center of the footing (Line A-A)

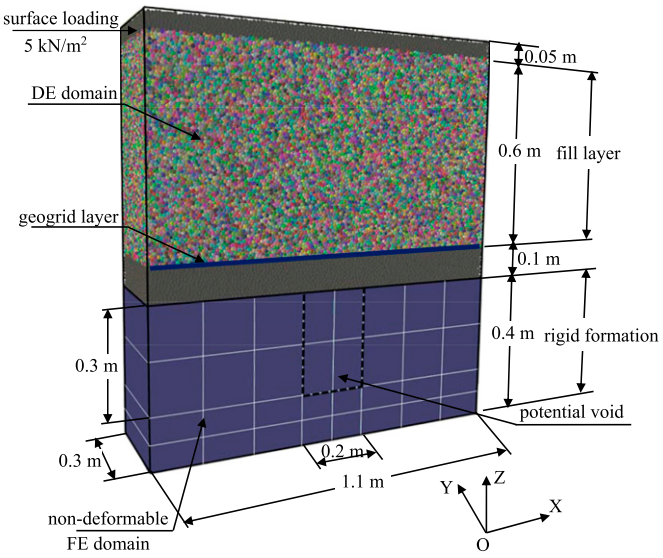

Fig. 14. Initial geometry of the geogrid-reinforced fill above the void

the soil, the geogrid was installed over a thin 0.1-m-thick soil layer overlying the nondeformable foundation, as shown in Fig. 14. A surcharge of 5 kN/m^2 was applied on top of the fill to simulate surface loading. This surcharge was modeled using a layer of 0.05-m-thick, high-density DE particles placed on top of the fill material. The cavity was assumed to develop after the fill placement was completed.

The soil properties used previously, and summarized in Table 1, were used for the fill material in the present numerical investigation. Similarly, the geogrid type (Tensar SS-0) was also used here as a reinforcement material. A preliminary study showed that a void width of 0.2 m results in negligible deformations in the soil and geogrid outside a region 0.45 m on each side from the void center line. Therefore, a total problem width of 1.1 m was deemed appropriate to capture the soil-geogrid interaction response above the induced void, as shown in Fig. 14.

The assembly was generated using the multilayer packing process described previously. The rigid formation was first modeled using nondeformable FEs. A 0.1-m-thick soil layer was then generated, followed by the introduction of the geogrid layer. The fill material was then generated in layers until the target height of 0.6 m was reached. A surcharge of 5 kN/m^2 was applied on top of the fill by using a layer (0.05 m thick) of high-density particles. The final assemblage consisted of over 280,000 DE particles and 2,800 FEs. After the material properties were assigned to all FEs and DEs, the geogrid was allowed to freely deform and interact with the soil. The initial condition of the modeled system was considered to be reached when the convergence criteria were satisfied (all internal and external forces were balanced). The final stage involved the void introduction by deactivating the FEs within the void area.

Downloaded from ascelibrary.org by McGill University on 08/08/16. Copyright ASCE. For personal use only; all rights reserved.

Response of the Geogrid

The calculated responses of the geogrid following the creation of the subsurface void are summarized in this section. The deformed shape of the geogrid is shown in Fig. 15. The maximum deformations and tensile stresses developed in the region immediately above the void. The geogrid was found to react to the loss of support and the associated soil movement by deforming downward, causing tensile stresses in the geogrid material. The distributions of the vertical displacements and tensile stresses in the geogrid resulting from the void introduction are shown in Fig. 16, where it can be seen that the vertical displacements and tensile stresses are generally small near the ends of the geogrid and reach maximum values near the void center. To examine the importance of the interlocking effect on the geogrid response a parametric study was performed, where the interface friction coefficient between the soil and geogrid was incrementally reduced. It was found that even when the friction coefficient reached zero the geogrid anchoring mechanism was still ensured with only a small increase in geogrid vertical displacement. This demonstrates the dominant role of the interlocking effect on the geogrid behavior. A similar observation related to the importance of interlocking effect was reported by Bridle et al. (1994).

Response of the Reinforced Soil

The calculated responses of the surrounding soil following the creation of the subsurface void are summarized in this section. The displacement fields in the fill layer with and without the presence of geogrid reinforcement are shown in Fig. 17. For unreinforced fill [Fig. 17(a)], downward soil movement occurred above the void

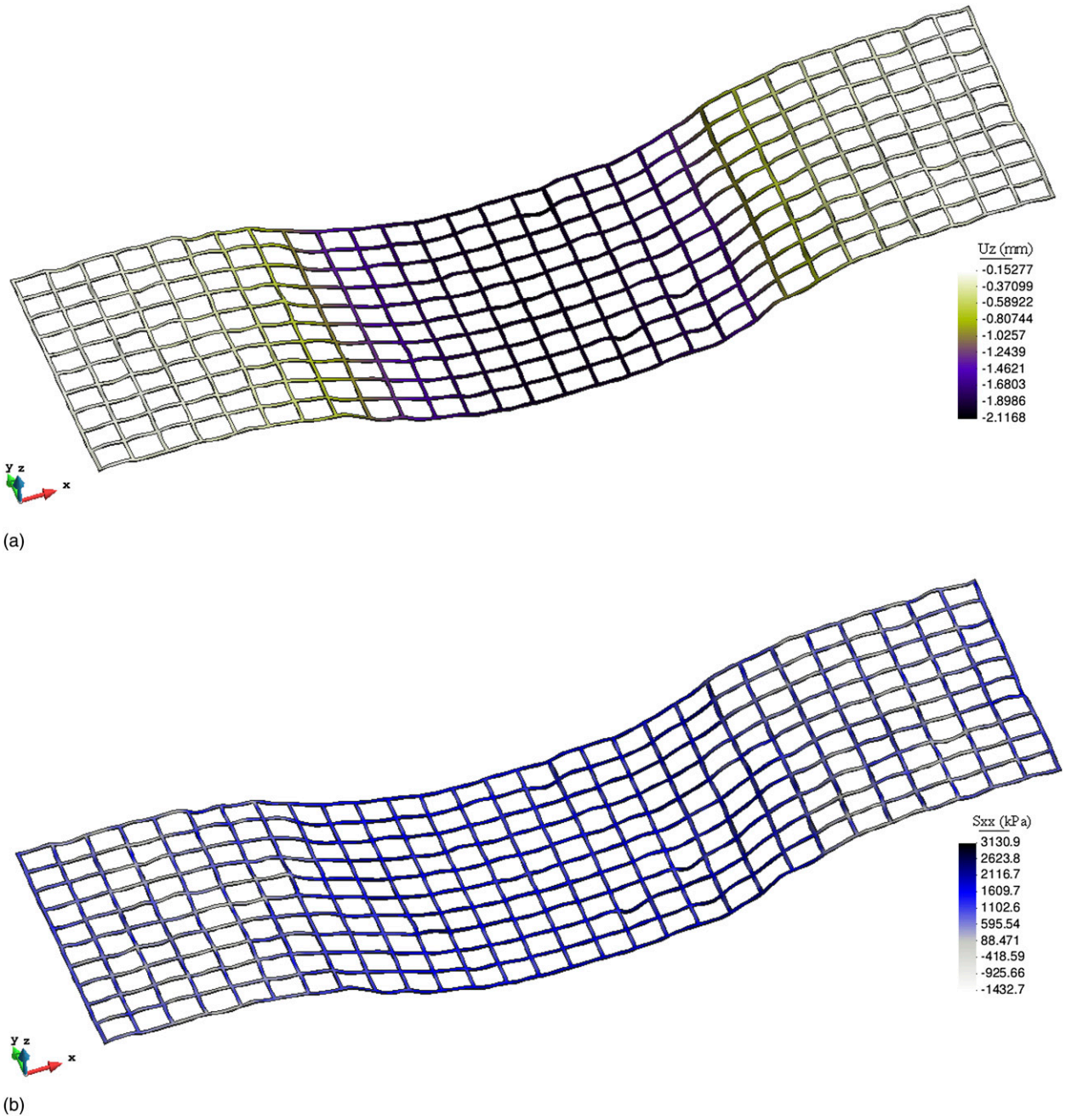

Fig. 15. (a) Vertical displacements and (b) tensile stresses in the geogrid

Downloaded from ascelibrary.org by McGill University on 08/08/16. Copyright ASCE. For personal use only; all rights reserved.

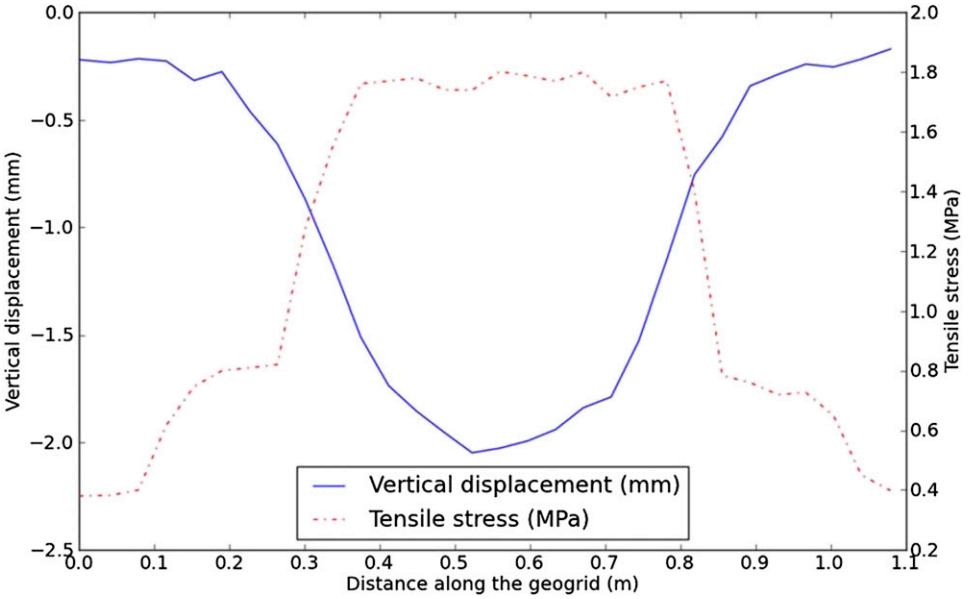

Fig. 16. Changes in vertical displacement and tensile stress along the geogrid

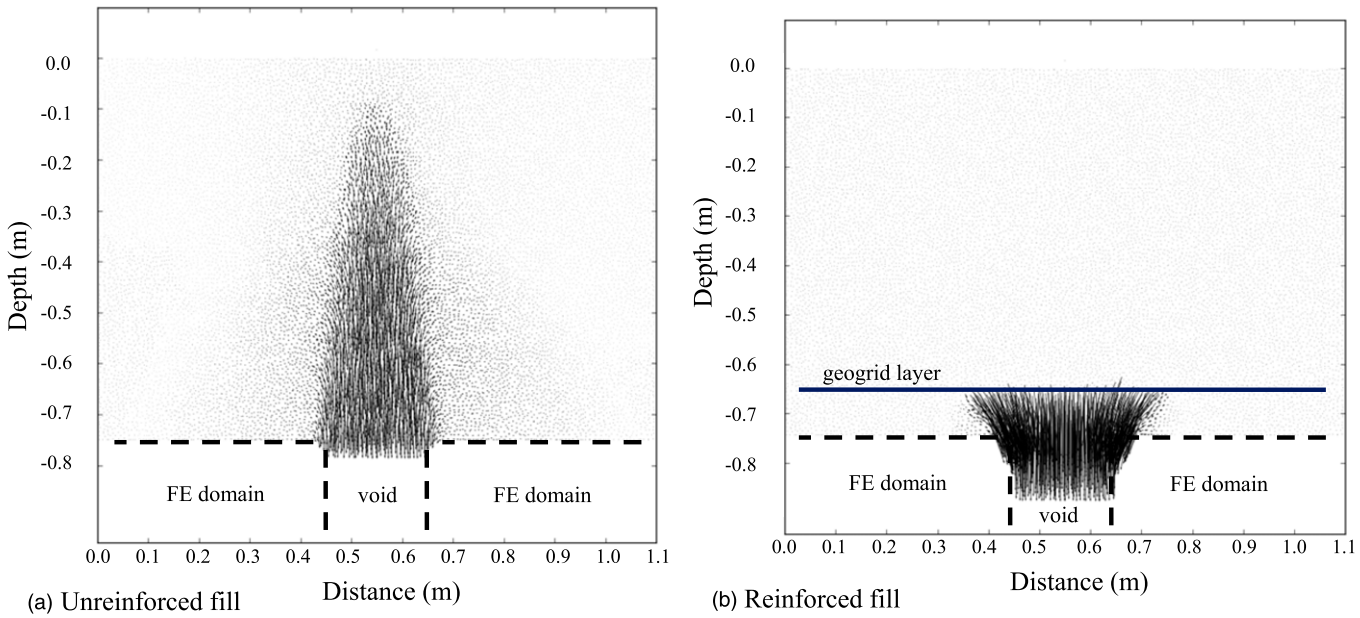

Fig. 17. Soil displacement fields as a result of void introduction

location followed by soil arching over the void. Fig. 17(b) shows the displacement field for the case of geogrid-reinforced fill, where it can be seen that soil displacements above the geogrid layer are much smaller compared with those calculated for the unreinforced fill. It is also seen that the geogrid soil-interaction plays an important role in preventing the soil from moving toward the void. This demonstrates the efficiency of the interlocking mechanism in generating a stiffened granular layer above the geogrid (Bridle et al. 1994).

The DE contact distributions were obtained by considering all contacts in the soil volume above the geogrid level. For unreinforced fill, the contact orientations in Fig. 18(a) show the development of soil arching within the fill with an anisotropic distribution such that there are more contacts in the horizontal x-direction than in the vertical z-direction (xz-plane view). The distribution of contacts in the yz-plane is found to be elliptical, with the z-component being slightly larger than the y-component. Meanwhile, quite uniform distribution of contact orientation is observed in the xy-plane. In Fig. 18(b), with the geogrid placement above the void, the distribution of contact orientations in the xz-plane show less arching with only a slightly larger contact value in the horizontal direction. Uniform contact distributions in the yz- and xy-planes are also observed. The presence of geogrid reinforcement is found to prevent contact rearrangement in the soil above the geogrid level. Soil deformation can also be evaluated by analyzing the change in porosity, which is obtained by comparing the change in the volume of DE particles within a reference volume measuring $S_x \times S_y \times S_z = 0.1 \times 0.3 \times 0.1$ m. The changes in porosity

Downloaded from ascelibrary.org by McGill University on 08/08/16. Copyright ASCE. For personal use only; all rights reserved.

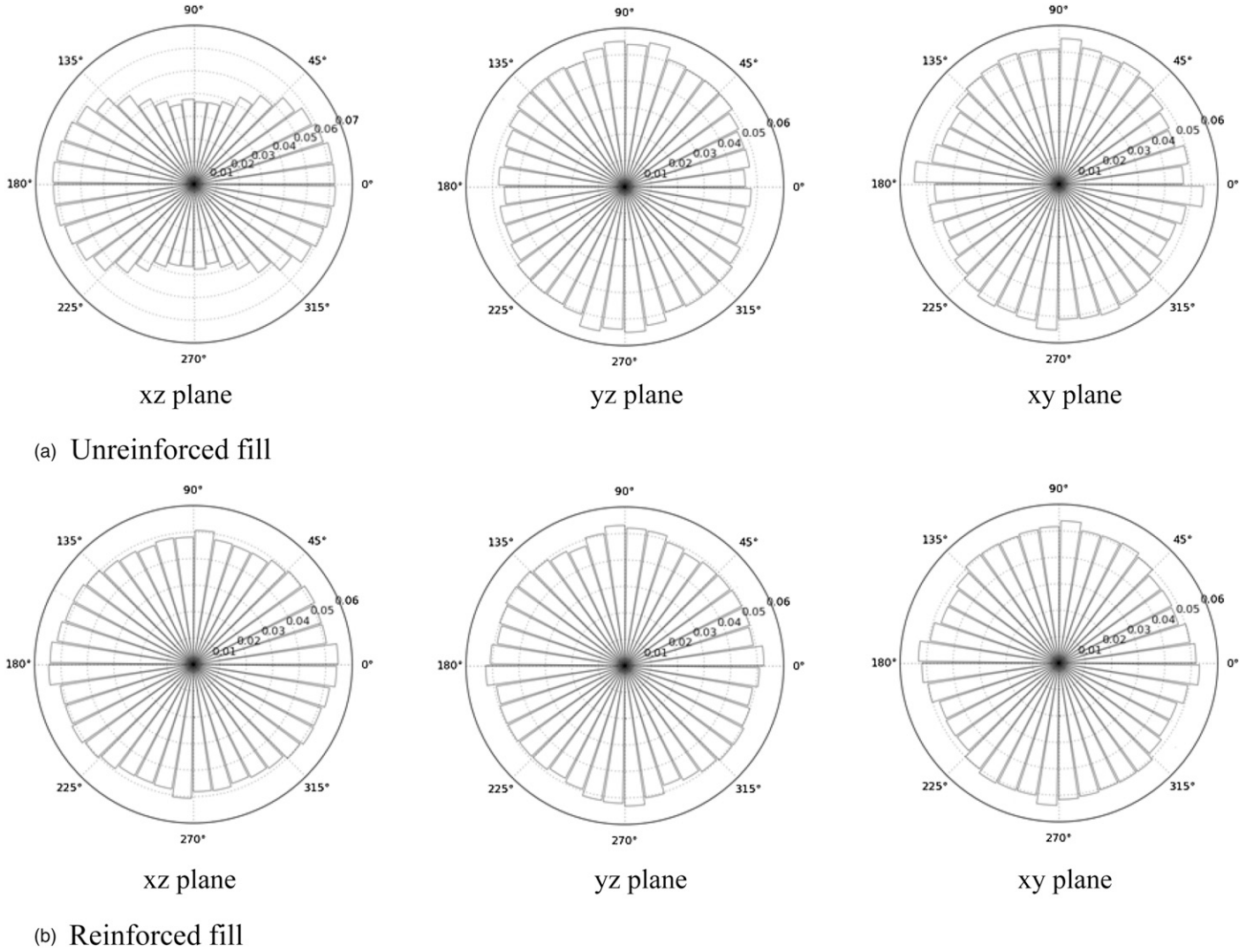

Fig. 18. Distributions of the contact orientation

for the unreinforced and reinforced cases are shown in Figs. 19(a and b), respectively. In both cases, there is an increase in porosity corresponding to volumetric dilation within the fill material. The maximum dilations occurred above the void location. Up to 10% porosity changes were observed in the unreinforced fill while much smaller changes (less than 1.1%) were observed in the geogrid-reinforced fill. A similar volumetric dilation in the fill was also reported by Costa et al. (2009) and Han et al. (2012).

The development of soil arching resulted in stress redistribution in the soil mass. The average stresses in the fill were calculated using a sampling volume with dimensions $S_x \times S_y \times S_z = 0.05 \times 0.3 \times 0.05$ m. The vertical and horizontal stress components calculated in the unreinforced and reinforced fill are shown in Figs. 20 and 21, respectively. A reduction of both the vertical and horizontal stresses above the void location was found in both cases. Vertical stresses increased in the regions adjacent to the void while horizontal stresses reached maximum values at the top of the soil layer as a result of the soil arching.

Summary and Conclusions

This study investigated numerically the 3D interaction between geogrid reinforcement and the surrounding soil using the coupled FE-DE framework. The soil was modeled using DEs while the geogrid was modeled using FEs. The interaction between the DE and FE domains was ensured by using interface elements. The computational cost was optimized by applying a multiple-time-step scheme during the analysis. The developed framework was used to investigate two geotechnical problems, namely, strip footing over geogrid-reinforced sand and geogrid-reinforced fill over a subsurface void. The soil-geogrid interlocking effect was demonstrated in the two investigated problems. The numerical simulations captured qualitative expectations for the two scenarios. The 3D geometry of the geogrid, its deformation, and stress distribution were represented. The microscopic behavior of the soil domain relative to the soil displacements, contact orientations, contact forces, and porosity changes was also examined.

The numerical modeling of the geogrid-reinforced strip footing provided very good agreement with the experimental results. Increasing the number of geogrid layers resulted in an increase in the ultimate bearing capacity of the supporting soil. The geogrid deformations and tensile stresses for $N = 1$ were larger than those for $N = 2$. When two layers of geogrid were used, the upper layer was found to experience larger deformations and tensile stresses compared with the lower layer. At the ultimate load, punching shear failure occurred above the geogrid followed by a general

Downloaded from ascelibrary.org by McGill University on 08/08/16. Copyright ASCE. For personal use only; all rights reserved.

Downloaded from ascelibrary.org by McGill University on 08/08/16. Copyright ASCE. For personal use only; all rights reserved.

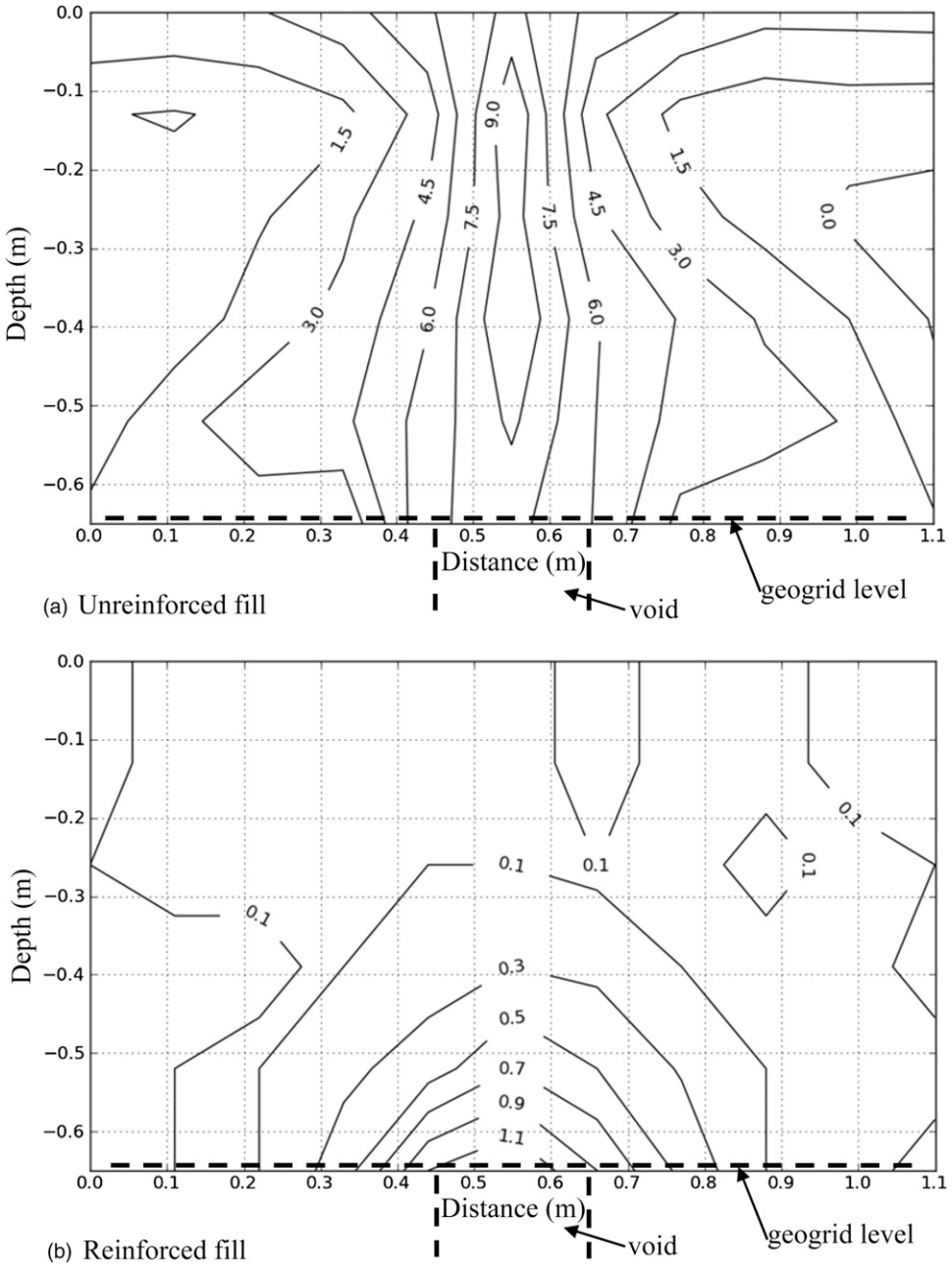

Fig. 19. Percentage changes in porosity in both unreinforced and reinforced fills

shear failure below the geogrid. The use of geogrid reinforcement also resulted in an increase in the vertical stresses in the supported soil.

The use of geogrid to reinforce a fill material subjected to a subsurface void within the supporting foundation was investigated using the FE-DE method. The presence of a geogrid layer was found to prevent soil from caving into the induced void, and therefore the stability of the fill was improved. The change in porosity in the reinforced fill was found to be significantly smaller than that for the unreinforced case. The development of soil arching and stress redistribution within the fill resulted in a reduction in vertical and horizontal stresses above the void location. Finally, the proposed coupled FE-DE method is proven to be effective in capturing the soil-geogrid interaction with detailed 3D responses of both the geogrid and the surrounding backfill material.

Acknowledgments

This research is supported by a research grant from the Natural Sciences and Engineering Research Council of Canada (NSERC). The financial support provided by a McGill Engineering Doctoral Award (MEDA) to V. D. H. T. is greatly appreciated.

Notation

The following symbols are used in this paper:

B = width of the strip foundation;
c = damping coefficient;
D_{50} = particle diameter corresponding to 50% passing;
E = particle material modulus, Young's modulus;

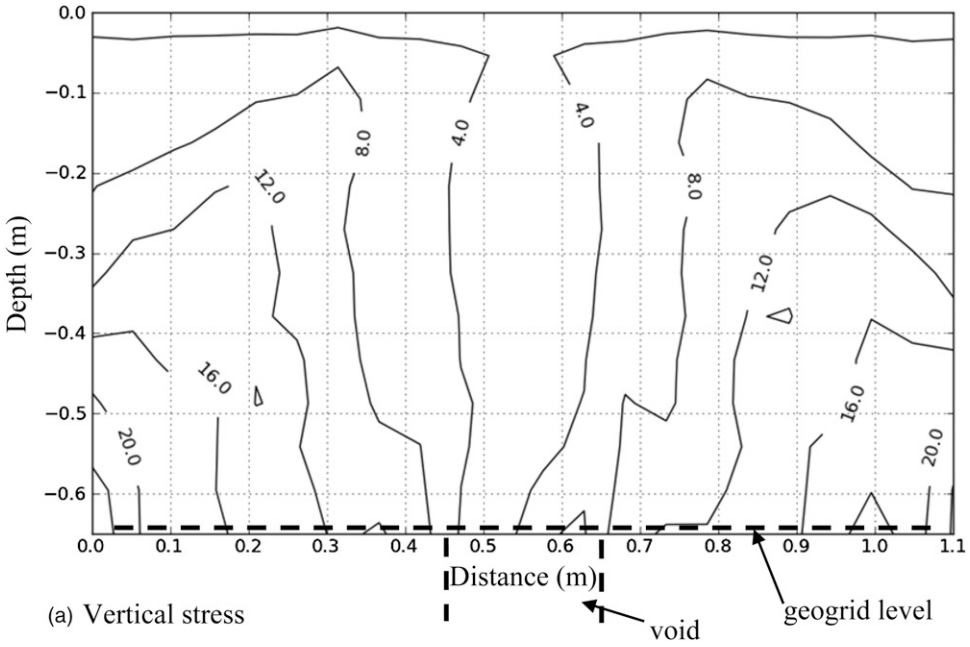

Fig. 20. Stress distributions in the unreinforced fill

$\mathbf{F}_{\text{contact}}$ = total contact force;
$\mathbf{F}_N$ = normal force of a contact;
$\mathbf{F}_T$ = tangential force of a contact;
$f^{c,j}$ = contact force vector at contact c;
$\mathbf{K}$ = stiffness matrix;
K_N = normal stiffness at the contact;
K_r = rolling stiffness of the interaction;
K_T = tangential stiffness at the contact;
$\mathbf{M}$ = mass matrix;
$\mathbf{M}_r$ = rolling resistance moment;
N = number of geogrid layers;
N_c = number of contacts;
N_i = shape function;
n_i = unit branch vector component;
$\mathbf{P}$ = external force vector;
q = foundation pressure;
r = particle radius;
V = volume of a measurement box;
$\mathbf{x}$ = displacement vector;
$x^{c,j}$ = branch vector connecting two contact particles;
$x^{(i)}$ = coordinate of node i;
$x^{(O)}$ = temporary center node;
α = constant ratio;
β_r = rolling resistance coefficient;
Δ_N = normal penetration between two particles;
Δt_{DE} = time step in the discrete-element domain;
Δt_{FE} = time step in the finite-element domain;
$\delta\Delta_T$ = incremental tangential displacement;
η_r = dimensionless coefficient;
θ_r = rolling angular vector;

Int. J. Geomech., 2015, 15(4): 04014066

Downloaded from ascelibrary.org by McGill University on 08/08/16. Copyright ASCE. For personal use only; all rights reserved.

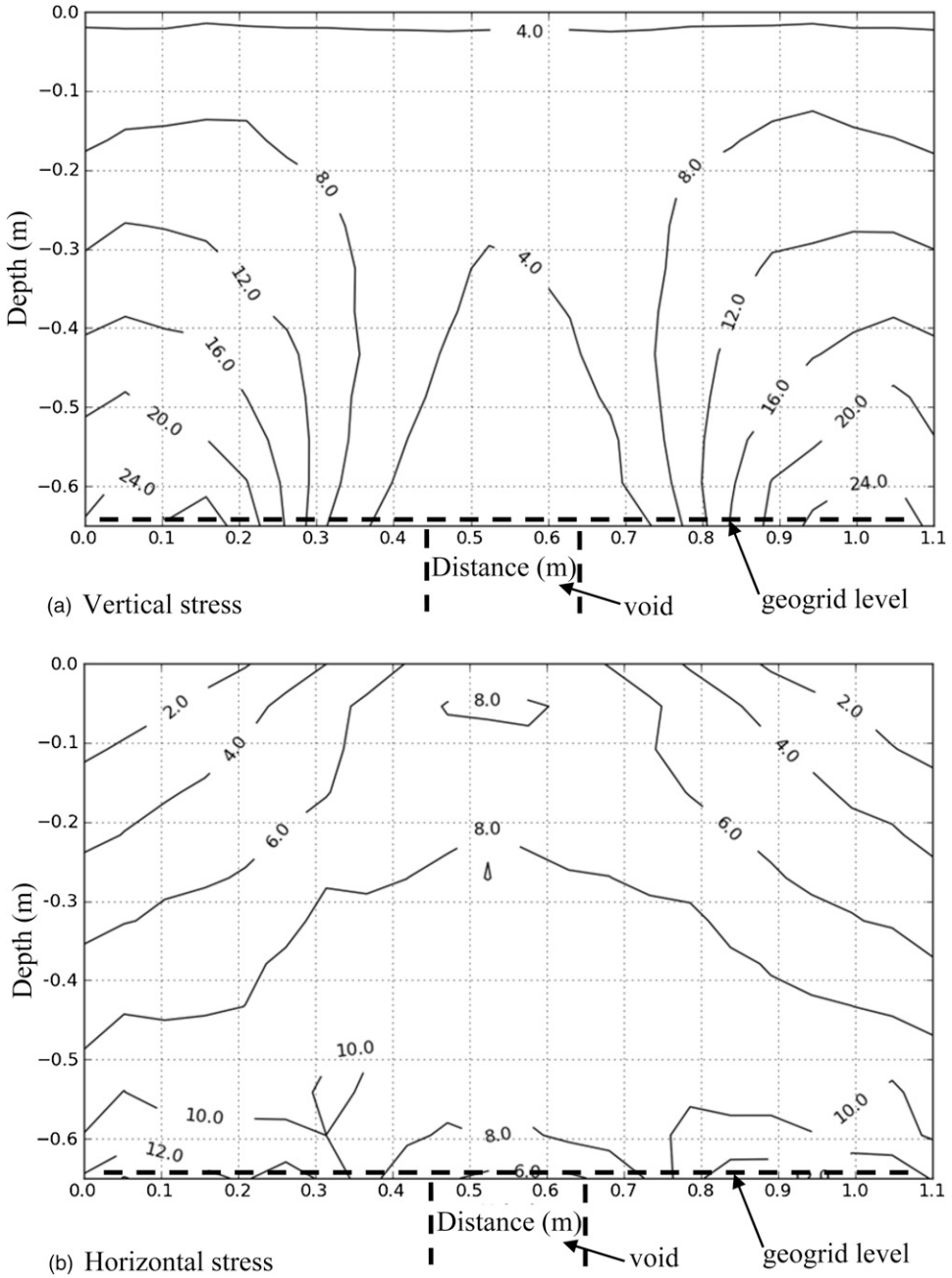

Fig. 21. Stress distributions in the reinforced fill

λ_m = maximum eigenvalue;
ν = Poisson's ratio;
σ = current pressure;
σ_{ij} = average stresses within a box;
Φ_{ij} = fabric tensor;
ϕ = friction angle; and
ϕ_{micro} = microscopic friction angle.

References

Abu-Farsakh, M., Chen, Q., Sharma, R., and Zhang, X. (2008). "Large-scale model footing tests on geogrid-reinforced foundation and marginal embankment soils." *Geotech. Test. J.*, 31(5), 413–423.

Adams, M. T., and Collin, J. G. (1997). "Large model spread footing load tests on geosynthetic reinforced soil foundations." *J. Geotech. Geoenviron. Eng.*, 10.1061/(ASCE)1090-0241(1997)123:1(66), 66–72.

Agaiby, S. W., and Jones, C. J. (1995). "Design of reinforced fill systems over voids." *Can. Geotech. J.*, 32(6), 939–945.

Basudhar, P. K., Saha, S., and Deb, K. (2007). "Circular footings resting on geotextile-reinforced sand bed." *Geotext. Geomembr.*, 25(6), 377–384.

Belheine, N., Plassiard, J. P., Donzé, F. V., Darve, F., and Seridi, A. (2009). "Numerical simulation of drained triaxial test using 3D discrete element modeling." *Comput. Geotech.*, 36(1–2), 320–331.

Binquet, J., and Lee, K. L. (1975a). "Bearing capacity analysis of reinforced earth slabs." *J. Geotech. Engrg. Div.*, 101(12), 1257–1276.

Binquet, J., and Lee, K. L. (1975b). "Bearing capacity tests on reinforced earth slabs." *J. Geotech. Engrg. Div.*, 101(12), 1241–1255.

Downloaded from ascelibrary.org by McGill University on 08/08/16. Copyright ASCE. For personal use only; all rights reserved.

Briançon, L., and Villard, P. (2008). "Design of geosynthetic-reinforced platforms spanning localized sinkholes." *Geotext. Geomembr.*, 26(5), 416–428.
Bridle, R. J., Jenner, C. G., and Barr, B. (1994). "Novel applications of geogrids in areas of shallow mine workings." *Proc., 5th Int. Conf. on Geotextiles, Geomembranes and Related Products*, Vol. 1, Southeast Asia Chapter of the Int. Geotextile Society (SEAC-IGS), Singapore, 297–300.
Chakraborty, D. and Kumar, J. (2014). "Bearing capacity of strip foundations in reinforced soils." *Int. J. Geomech.*, 10.1061/(ASCE)GM.1943-5622.0000275, 45–58.
Chen, C., McDowell, G. R., and Thom, N. H. (2012). "Discrete element modelling of cyclic loads of geogrid-reinforced ballast under confined and unconfined conditions." *Geotext. Geomembr.*, 35, 76–86.
Chen, Q., Abu-Farsakh, M., and Sharma, R. (2009). "Experimental and analytical studies of reinforced crushed limestone." *Geotext. Geomembr.*, 27(5), 357–367.
Chen, Q., Abu-Farsakh, M. Y., Sharma, R., and Zhang, X. (2007). "Laboratory investigation of behavior of foundations on geosynthetic-reinforced clayey soil." *Transportation Research Record 2004*, Transportation Research Board, Washington, DC, 28–38.
Choudhary, A. K., Jha, J. N., and Gill, K. S. (2010). "Laboratory investigation of bearing capacity behaviour of strip footing on reinforced flyash slope." *Geotext. Geomembr.*, 28(4), 393–402.
Chung, W., and Cascante, G. (2007). "Experimental and numerical study of soil-reinforcement effects on the low-strain stiffness and bearing capacity of shallow foundations." *Geotech. Geol. Eng.*, 25(3), 265–281.
Costa, Y. D., Zornberg, J. G., Bueno, B. S., and Costa, C. L. (2009). "Failure mechanisms in sand over a deep active trapdoor." *J. Geotech. Geoenviron. Eng.*, 10.1061/(ASCE)GT.1943-5606.0000134, 1741–1753.
Cundall, P. A., and Strack, O. D. (1979). "A discrete numerical model for granular assemblies." *Geotechnique*, 29(1), 47–65.
Dang, H. K., and Meguid, M. A. (2010a). "Algorithm to generate a discrete element specimen with predefined properties." *Int. J. Geomech.*, 10.1061/(ASCE)GM.1943-5622.0000028, 85–91.
Dang, H. K., and Meguid, M. A. (2010b). "Evaluating the performance of an explicit dynamic relaxation technique in analyzing nonlinear geotechnical engineering problems." *Comput. Geotech.*, 37(1–2), 125–131.
Dang, H. K., and Meguid, M. A. (2013). "An efficient finite–discrete element method for quasi-static nonlinear soil–structure interaction problems." *Int. J. Numer. Anal. Methods Geomech.*, 37(2), 130–149.
Das, B. M., Shin, E. C., and Omar, M. T. (1994). "The bearing capacity of surface strip foundations on geogrid-reinforced sand and clay—A comparative study." *Geotech. Geol. Eng.*, 12(1), 1–14.
Dash, S. K., Krishnaswamy, N. R., and Rajagopal, K. (2001). "Bearing capacity of strip footings supported on geocell-reinforced sand." *Geotext. Geomembr.*, 19(4), 235–256.
DeMerchant, M. R., Valsangkar, A. J., and Schriver, A. B. (2002). "Plate load tests on geogrid-reinforced expanded shale lightweight aggregate." *Geotext. Geomembr.*, 20(3), 173–190.
Elmekati, A., and El Shamy, U. (2010). "A practical co-simulation approach for multiscale analysis of geotechnical systems." *Comput. Geotech.*, 37(4), 494–503.
Ferellec, J. F., and McDowell, G. R. (2012). "Modelling of ballast–geogrid interaction using the discrete-element method." *Geosynth. Int.*, 19(6), 470–479.
Gabr, M. A., and Hunter, T. J. (1994). "Stress-strain analysis of geogrid-supported liners over subsurface cavities." *Geotech. Geol. Eng.*, 12(2), 65–86.
Gabr, M. A., Hunter, T. J., and Collin, J. G. (1992). "Stability of geogrid-reinforced landfill liners over sinkholes." *Proc., Earth Reinforcement Practice*, H. Ochiai, S. Hayashi, and J. Otani, eds., Balkema, Rotterdam, Netherlands, 595–600.
Gaetano, E. A. (2010). "The response of flexible pavement systems to local deterioration of the base layer." M.S. thesis, McGill Univ., Montréal.
Ghazavi, M., and Lavasan, A. A. (2008). "Interference effect of shallow foundations constructed on sand reinforced with geosynthetics." *Geotext. Geomembr.*, 26(5), 404–415.
Ghosh, A., and Dey, U. (2009). "Bearing ratio of reinforced fly ash overlying soft soil and deformation modulus of fly ash." *Geotext. Geomembr.*, 27(4), 313–320.
Giroud, J. P., Bonaparte, R., Beech, J. F., and Gross, B. A. (1990). "Design of soil layer-geosynthetic systems overlying voids." *Geotext. Geomembr.*, 9(1), 11–50.
Guido, V. A., Chang, D. K., and Sweeny, M. A. (1986). "Comparison of geogrid and geotextile reinforced slabs." *Can. Geotech. J.*, 23(4), 435–440.
Halvordson, K. A., Plaut, R. H., and Filz, G. M. (2010). "Analysis of geosynthetic reinforcement in pile-supported embankments. Part II: 3D cable-net model." *Geosynth. Int.*, 17(2), 68–76.
Han, J., Bhandari, A., and Wang, F. (2012). "DEM analysis of stresses and deformations of geogrid-reinforced embankments over piles." *Int. J. Geomech.*, 10.1061/(ASCE)GM.1943-5622.0000050, 340–350.
Huang, C. C., and Menq, F. Y. (1997). "Deep-footing and wide-slab effects in reinforced sandy ground." *J. Geotech. Geoenviron. Eng.*, 10.1061/(ASCE)1090-0241(1997)123:1(30), 30–36.
Huang, C. C., and Tatsuoka, F. (1990). "Bearing capacity of reinforced horizontal sandy ground." *Geotext. Geomembr.*, 9(1), 51–82.
Jenck, O., Dias, D., and Kastner, R. (2009). "Three-dimensional numerical modeling of a piled embankment." *Int. J. Geomech.*, 10.1061/(ASCE)1532-3641(2009)9:3(102), 102–112.
Jeon, S. S. (2011). "Vertical earth pressure increments due to vibratory roller on geogrid-reinforced embankments." *Geosynth. Int.*, 18(5), 332–338.
Jiang, M. J., Konrad, J. M., and Leroueil, S. (2003). "An efficient technique for generating homogeneous specimens for DEM studies." *Comput. Geotech.*, 30(7), 579–597.
Jones, B. M., Plaut, R. H., and Filz, G. M. (2010). "Analysis of geosynthetic reinforcement in pile-supported embankments. Part I: 3D plate model." *Geosynth. Int.*, 17(2), 59–67.
Khing, K. H., Das, B. M., Puri, V. K., Cook, E. E., and Yen, S. C. (1993). "The bearing-capacity of a strip foundation on geogrid-reinforced sand." *Geotext. Geomembr.*, 12(4), 351–361.
Kinney, T. C., and Connor, B. (1987). "Geosynthetics supporting embankments over voids." *J. Cold Reg. Eng.*, 10.1061/(ASCE)0887-381X(1987)1:4(158), 158–170.
Koutsabeloulis, N. C., and Griffiths, D. V. (1989). "Numerical modelling of the trap door problem." *Geotechnique*, 39(1), 77–89.
Kozicki, J., and Donzé, V. F. (2009). "*YADE-OPEN DEM*: An open-source software using a discrete element method to simulate granular material." *Eng. Comput.*, 26(7), 786–805.
Kumar, A., and Saran, S. (2003). "Bearing capacity of rectangular footing on reinforced soil." *Geotech. Geol. Eng.*, 21(3), 201–224.
Kurian, N. P., Beena, K. S., and Kumar, R. K. (1997). "Settlement of reinforced sand in foundations." *J. Geotech. Geoenviron. Eng.*, 10.1061/(ASCE)1090-0241(1997)123:9(818), 818–827.
Kwon, J., Tutumluer, E., and Konietzky, H. (2008). "Aggregate base residual stresses affecting geogrid reinforced flexible pavement response." *Int. J. Pavement Eng.*, 9(4), 275–285.
Labra, C., and Oñate, E. (2009). "High density sphere packing for discrete element method simulations." *Commun. Numer. Methods Eng.*, 25(7), 837–849.
Lawson, C. R., Jones, C. J. F. P., Kempton, G. T., and Passaris, E. K. S. (1994). "Advanced analysis of reinforced fills over areas prone to subsidence." *Proc., 5th Int. Conf. on Geotextiles, Geomembranes and Related Products*, Vol. 1, Balkema, Rotterdam, Netherlands, 311–317.
Li, F. L., Peng, F. L., Tan, Y., Kongkitkul, W., and Siddiquee, M. S. A. (2012). "FE simulation of viscous behavior of geogrid-reinforced sand under laboratory-scale plane-strain-compression testing." *Geotext. Geomembr.*, 31(4), 72–80.
Lin, Y. L., Zhang, M. X., Javadi, A. A., Lu, Y., and Zhang, S. L. (2013). "Experimental and DEM simulation of sandy soil reinforced with H-V inclusions in plane strain tests." *Geosynth. Int.*, 20(3), 162–173.
Liu, H. L., Ng, C. W., and Fei, K. (2007). "Performance of a geogrid-reinforced and pile-supported highway embankment over soft clay: Case study." *J. Geotech. Geoenviron. Eng.*, 10.1061/(ASCE)1090-0241(2007)133:12(1483), 1483–1493.
Lobo-Guerrero, S., and Vallejo, L. E. (2006). "Discrete element method analysis of railtrack ballast degradation during cyclic loading." *Granular Matter*, 8(3–4), 195–204.

Downloaded from ascelibrary.org by McGill University on 08/08/16. Copyright ASCE. For personal use only; all rights reserved.

Madhavi Latha, G. M., and Somwanshi, A. (2009a). "Bearing capacity of square footings on geosynthetic reinforced sand." *Geotext. Geomembr.*, 27(4), 281–294.

Madhavi Latha, G. M., and Somwanshi, A. (2009b). "Effect of reinforcement form on the bearing capacity of square footings on sand." *Geotext. Geomembr.*, 27(6), 409–422.

Maynar, M. J., and Rodríguez, L. E. (2005). "Discrete numerical model for analysis of earth pressure balance tunnel excavation." *J. Geotech. Geoenviron. Eng.*, 10.1061/(ASCE)1090-0241(2005)131:10(1234), 1234–1242.

McDowell, G. R., Harireche, O., Konietzky, H., Brown, S. F., and Thom, N. H. (2006). "Discrete element modelling of geogrid-reinforced aggregates." *Proc. Inst. Civ. Eng. Geotech. Eng.*, 159(1), 35–48.

Meguid, M. A., and Dang, H. K. (2009). "The effect of erosion voids on existing tunnel linings." *Tunnelling Underground Space Technol.*, 24(3), 278–286.

Meyerhof, G. G., and Hanna, A. M. (1978). "Ultimate bearing capacity of foundations on layered soils under inclined load." *Can. Geotech. J.*, 15(4), 565–572.

Michalowski, R. L. (2004). "Limit loads on reinforced foundation soils." *J. Geotech. Geoenviron. Eng.*, 10.1061/(ASCE)1090-0241(2004)130:4(381), 381–390.

Michalowski, R. L., and Shi, L. (2003). "Deformation patterns of reinforced foundation sand at failure." *J. Geotech. Geoenviron. Eng.*, 10.1061/(ASCE)1090-0241(2003)129:6(439), 439–449.

Moghaddas Tafreshi, S. N., and Dawson, A. R. (2010). "Behaviour of footings on reinforced sand subjected to repeated loading—Comparing use of 3D and planar geotextile." *Geotext. Geomembr.*, 28(5), 434–447.

Moghaddas Tafreshi, S. N., Khalaj, O., and Halvaee, M. (2011). "Experimental study of a shallow strip footing on geogrid-reinforced sand bed above a void." *Geosynth. Int.*, 18(4), 178–195.

Mohamed, M. H. A. (2010). "Two dimensional experimental study for the behaviour of surface footings on unreinforced and reinforced sand beds overlying soft pockets." *Geotext. Geomembr.*, 28(6), 589–596.

Patra, C. R., Das, B. M., Bhoi, M., and Shin, E. C. (2006). "Eccentrically loaded strip foundation on geogrid-reinforced sand." *Geotext. Geomembr.*, 24(4), 254–259.

Poorooshasb, H. B. (1991). "Load settlement response of a compacted fill layer supported by a geosynthetic overlying a void." *Geotext. Geomembr.*, 10(3), 179–201.

Sadoglu, E., Cure, E., Moroglu, B., and Uzuner, B. A. (2009). "Ultimate loads for eccentrically loaded model shallow strip footings on geotextile-reinforced sand." *Geotext. Geomembr.*, 27(3), 176–182.

Schlosser, F., Jacobsen, H. M., and Juran, I. (1983). "Soil reinforcement—General report." *Proc., 8th European Conf. on Soil Mechanics and Foundation Engineering*, Balkema, Rotterdam, Netherlands, 83–103.

Sharma, R., Chen, Q., Abu-Farsakh, M., and Yoon, S. (2009). "Analytical modeling of geogrid reinforced soil foundation." *Geotext. Geomembr.*, 27(1), 63–72.

Shin, E. C., Das, B. M., Puri, V. K., Yen, S. C., and Cook, E. E. (1993). "Bearing capacity of strip foundation on geogrid-reinforced clay." *Geotech. Test. J.*, 16(4), 534–541.

Siddiquee, M. S. A., and Huang, C. C. (2001). "FEM simulation of the bearing capacity of level reinforced sand ground subjected to footing load." *Geosynth. Int.*, 8(6), 501–549.

Šmilauer, V., et al. (2010). "Welcome to *YADE*—Open source discrete element method." ⟨http://yade-dem.org/doc/⟩ (Dec. 15, 2013).

Terzaghi, K. (1936). "Stress distribution in dry and saturated sand above a yielding trap door." *Proc., Int. Conf. of Soil Mechanics*, Vol. 1, Harvard Univ., Cambridge, MA, 307–311.

Tran, V. D. H., Meguid, M. A., and Chouinard, L. E. (2013). "A finite–discrete element framework for the 3D modeling of geogrid–soil interaction under pullout loading conditions." *Geotext. Geomembr.*, 37(1), 1–9.

Tran, V. D. H., Meguid, M. A., and Chouinard, L. E. (2014). "Discrete element and experimental investigations of the earth pressure distribution on cylindrical shafts." *Int. J. Geomech.*, 10.1061/(ASCE)GM.1943-5622.0000277, 80–91.

Villard, P., Chevalier, B., Hello, B. L., and Combe, G. (2009). "Coupling between finite and discrete element methods for the modelling of earth structures reinforced by geosynthetic." *Comput. Geotech.*, 36(5), 709–717.

Villard, P., Gourc, J. P., and Giraud, H. (2000). "A geosynthetic reinforcement solution to prevent the formation of localized sinkholes." *Can. Geotech. J.*, 37(5), 987–999.

Wang, F., Han, J., Miao, L.-C., and Bhandari, A. (2009). "Numerical analysis of geosynthetic-bridged and drilled shafts-supported embankments over large sinkholes." *Geosynth. Int.*, 16(6), 408–419.

Wang, M. C., Feng, Y. X., and Jao, M. (1996). "Stability of geosynthetic-reinforced soil above a cavity." *Geotext. Geomembr.*, 14(2), 95–109.

Wayne, M. H., Han, J., and Akins, K. (1998). "The design of geosynthetic reinforced foundations." *Proc., Annual Convention and Exposition*, Geotechnical Special Publication, Vol. 76, ASCE, New York, 1–18.

Xiao, S. P., and Belytschko, T. (2004). "A bridging domain method for coupling continua with molecular dynamics." *Comput. Meth. Appl. Mech. Eng.*, 193(17–20), 1645–1669.

Yamamoto, K., and Otani, J. (2002). "Bearing capacity and failure mechanism of reinforced foundations based on rigid-plastic finite element formulation." *Geotext. Geomembr.*, 20(6), 367–393.

Yetimoglu, T., Wu, J. T. H., and Saglamer, A. (1994). "Bearing capacity of rectangular footings on geogrid-reinforced sand." *J. Geotech. Engrg.*, 10.1061/(ASCE)0733-9410(1994)120:12(2083), 2083–2099.

Downloaded from ascelibrary.org by McGill University on 08/08/16. Copyright ASCE. For personal use only; all rights reserved.